Numerical Simulation of the 2011 Tohoku Tsunami Based on a New Transient FEM Co-seismic Source: Comparison to Far- and Near-Field Observations

STEPHAN T. GRILLI,[1] JEFFREY C. HARRIS,[1] TAYEBEH S. TAJALLI BAKHSH,[1] TIMOTHY L. MASTERLARK,[2] CHRISTODOULOS KYRIAKOPOULOS,[3] JAMES T. KIRBY,[4] and FENGYAN SHI[4]

Abstract—In this work, we simulate the 2011 M9 Tohoku-Oki tsunami using new coseismic tsunami sources based on inverting onshore and offshore geodetic data, using 3D Finite Element Models (FEM). Such FEMs simulate elastic dislocations along the plate boundary interface separating the stiff subducting Pacific Plate from the relatively weak forearc and volcanic arc of the overriding Eurasian plate. Due in part to the simulated weak forearc materials, such sources produce significant shallow slip (several tens of meters) along the updip portion of the rupture near the trench. To assess the accuracy of the new approach, we compare observations and numerical simulations of the tsunami's far- and near-field coastal impact for: (i) one of the standard seismic inversion sources (UCSB; SHAO et al. 2011); and (ii) the new FEM sources. Specifically, results of numerical simulations for both sources, performed using the fully nonlinear and dispersive Boussinesq wave model FUNWAVE-TVD, are compared to DART buoy, GPS tide gauge, and inundation/runup measurements. We use a series of nested model grids with varying resolution (down to 250 m nearshore) and size, and assess effects on model results of the latter and of model physics (such as when including dispersion or not). We also assess the effects of triggering the tsunami sources in the propagation model: (i) either at once as a hot start, or with the spatiotemporal sequence derived from seismic inversion; and (ii) as a specified surface elevation or as a more realistic time and space-varying bottom boundary condition (in the latter case, we compute the initial tsunami generation up to 300 s using the non-hydrostatic model NHWAVE). Although additional refinements are expected in the near future, results based on the current FEM sources better explain long wave near-field observations at DART and GPS buoys near Japan, and measured tsunami inundation, while they simulate observations at distant DART buoys as well or better than the UCSB source. None of the sources, however, are able to explain the largest runup and inundation measured between 39.5° and 40.25°N, which could be due to insufficient model resolution in this region (Sanriku/Ria) of complex bathymetry/topography, and/or to additional tsunami generation mechanisms not represented in the coseismic sources (e.g., splay faults, submarine mass failure). This will be the object of future work.

Key words: The Tohoku 2011 tsunami, tsunami source modeling by FEM with geodetic data assimilation, tsunami propagation modeling (near- and far-field) in a Boussinesq model, comparison of model results with surface elevation, runup, and inundation observations, wave dispersion effects, sensitivity analyses to boundary conditions, model physics, and grid parameters.

1. Introduction

On March 11th, 2011, at 2:46 pm JST (05:46 UTC) a massive earthquake of magnitude $M_w = 9.0$ struck near the northeastern coast of Japan (37°49′N, 143°03′E; Fig. 1), with substantial slip at fairly shallow depths (about 10–20 km), causing large seafloor motions that triggered very high tsunami waves. The main earthquake shocks lasted for 3–4 min and, owing to the proximity of the epicenter to shore, the first significant waves reached Japan only 10 min after the event started, thus allowing for very little warning time. The tsunami caused extensive and often near total destruction along the coast of the Tohoku region, between 35° and 43°N. Post-tsunami surveys of runups and inundation depths showed maximum values in the 20–40 m range mostly between 37.7° and 40.2°N, where the Miyagi and Iwate Prefectures are located (MORI et al. 2012). [The largest measured runup of 40.1 m occurred in a narrow valley of Ofunato (Iwate; 39.1N)]. The largest runups occurred in the north, along the Sanriku/Ria coast (located north of 37°N), which has a very complicated bathymetry and topography that tends to amplify tsunami impact. By contrast, the area located

---

[1] Department of Ocean Engineering, University of Rhode Island, Narragansett, RI, USA. E-mail: grilli@oce.uri.edu
[2] Department of Geological Sciences, The University of Alabama (UoA), Tuscaloosa, AL, USA.
[3] Instituto Nazionale di Geofisica e Vulcanologia, Rome, Italy.
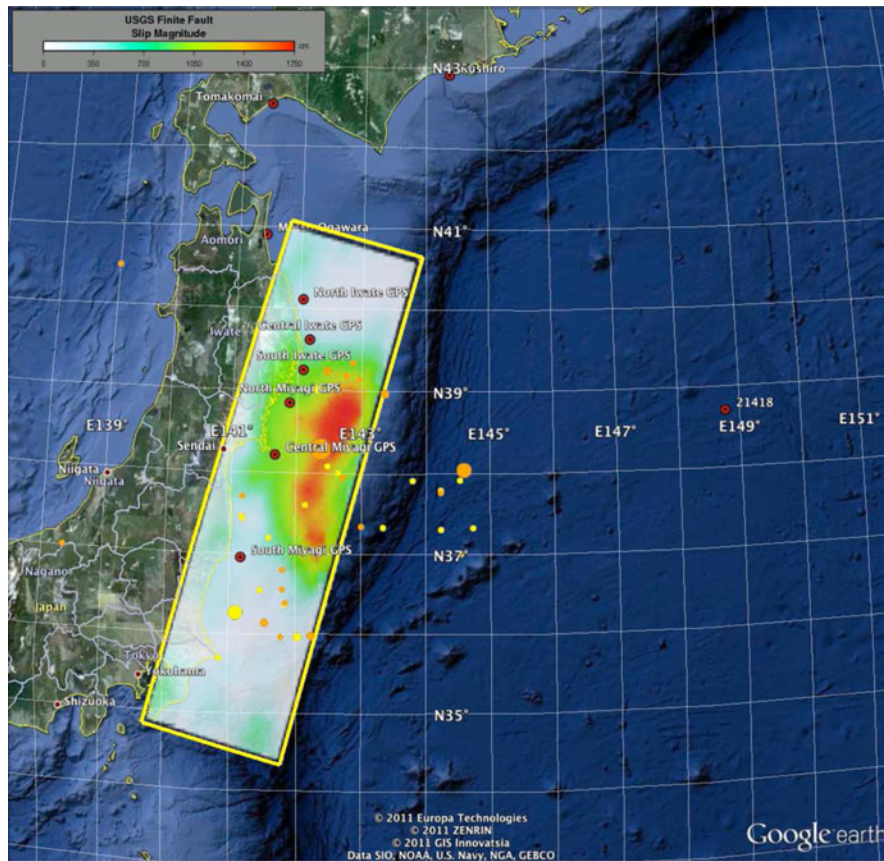[4] Center for Applied Coastal Research, University of Delaware, Newark, DE, USA.

Figure 1

Location and maximum slip magnitude (*color scale*) of USGS finite fault model source for the M9 Tohoku-Oki earthquake of March 11th, 2011, at 2:46 pm JST (05:46 UTC). *Plain yellow* and *orange circles* indicate the location of the main aftershocks (of varying depth (*color*) and magnitude (size)), during the first 10 h following the event (the largest symbol within the maximum slip area marks the epicenter). *Red dots* mark the location of nearshore GPS buoys (labeled) and the one DART buoy nearest Japan (labeled 21418 to the *right*). [The Tohoku region occupies the northeastern portion of Honshu, the largest island of Japan, approximately north of 36°N, and consists of six prefectures: Akita, Aomori, Fukushima, Iwate, Miyagi and Yamagata. The *darkest blue* area east of Tohoku denotes the expression of the Japan trench on the seafloor]

directly south, which mostly consists of plains, was less impacted by the tsunami. As a result of the tsunami, thousands of people in Japan lost their lives or were reported missing (nearly 16,000 and 4,000, respectively, with 99.6 % of those occurring in the Iwate Prefecture; only a very small percentage of casualties was directly caused by the earthquake), a large number of people were injured, and millions more were affected by the lack of water and food, electricity, and transportation (IOC/UNESCO, 2011). This dramatic outcome occurred despite the widespread coastal protections against tsunamis (e.g., seawalls and breakwaters), advanced early warning systems, and evacuation procedures that have been

installed, perfected, and rehearsed in Japan over the past few decades. Without these multiple measures, however, in view of the extreme size of this event, it is likely that the human toll in Japan would have been far worse.

Within one hour of the event, when the tsunami reached the nearest DART buoys (Deep-water Assessment and Reporting of Tsunami network; GONZALEZ *et al.* 1998; Fig. 1), propagation models of the anticipated far-field impact of the tsunami caused sufficient concern (particularly with the US Pacific Tsunami Warning Center; PTWC) to trigger evacuations and warnings in many distant areas across the Pacific Ocean. Large impact was predicted as far as

South America (e.g., Chile), where waves were expected to arrive after more than 20 h of propagation. In the meantime, through a chain of failures of coastal protections and back-up power systems caused by the earthquake and the tsunami inundation, the core of one of the reactors at the Fukushima Dai-Ichi nuclear power plant (near 37°25′N) started melting, eventually causing explosions that released large doses of radiation, and in the days following the event forcing a complete evacuation of all people living within tens of kilometers of the power plant that will likely last for many decades.

At least four historical events had been identified in paleo-tsunami and other records to have caused large coastal impact and runup in the Tohoku region: i.e., the 869 Jogan (with book records showing coastal inundations perhaps even greater than for the 2011 event), the 1611 Keicho Sanriku (tsunami height 6–8 m), the 1896 Meiji (maximum runup 38.2 m), and the 1933 Showa (maximum runup 29.2 m) tsunamis (HATORI 1975; ABE et al. 1990; MINOURA et al. 2001; SAWAI et al. 2008). These and other significant events were assembled into a compounded historical record of runup and inundation in the area, which closely resembles post-tsunami survey observations of the Tohoku tsunami impact (MORI et al. 2012). Based in part on such historical records and on knowledge of local tectonics, large earthquakes with magnitude as high as $M_{\mathrm{w}} \simeq 8.2$ had been expected for this area of Japan in the near future (although further south). However, the large magnitude of the Tohoku-Oki earthquake and especially of the generated tsunami were largely unexpected, at least by those in charge of tsunami hazard assessment and mapping in Japan.

This tsunami is indeed believed to have been the largest in Japan's recorded history (HAYASHI et al. 2011). The earthquake ruptured the boundary separating the subducting Pacific Plate from the overriding Okhotsk Plate (a small and narrow plate that is distinct from the North American Plate; SENO et al. 1996). This segment of the plate boundary intersects the seafloor at the Japan Trench (Fig. 2), where it dips about 10° to a down-dip distance of about 100 km from the trench. The dip of the subducting plate then increases along the seismogenic zone to the west (HASEGAWA et al. 2007). The rupture
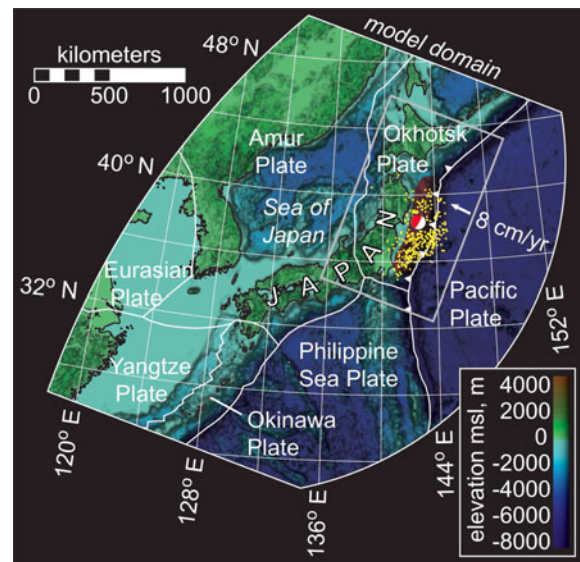

Figure 2
Seismotectonics of the M9 2011 Tohoku Earthquake. The surface projection of the rupture zone is marked by the *red polygon*. The epicenter is shown with the USGS CMT focal mechanism (see Fig. 1). *Yellow dots* are epicenters for $M > 4$ aftershocks, spanning 11 March through 6 May 2011. The Pacific-Okhotsk plate convergence is about 8 cm/year. Plate boundaries are modified from BIRD (2003)

area, 150 km east of Sendai, Japan, extends a few hundred km in the along strike direction, offshore of the Prefectures of Aomori, Miyagi, and Fukushima. At the latitude of the earthquake, the Pacific Plate moves approximately westward with respect to the Okhotsk Plate at a rate of 8 cm/year (DEMETS et al. 1994) (Fig. 2). The focal mechanisms reported by Harvard CMT, the U.S. Geological Survey (USGS), and the Earthquake Research Institute at the University of Tokyo, all indicated that the earthquake was predominantly thrust with a moment more than $M_{\mathrm{o}} \simeq 4.0 \times 10^{22}$ Nm, and a variety of seismic, geodetic, and tsunami genesis studies concluded that the magnitude was indeed $M_{\mathrm{w}} = 9.0$ (e.g., IDE et al. 2011; SIMONS et al. 2011). Some geodetic inversion models (e.g., OZAWA et al. 2011; POLLITZ et al. 2011) suggest that the peak slip may have exceeded 30–35 m in some areas, while some seismic inversion models suggest over 50–60 m of maximum slip (e.g., AMMON et al. 2011; SHAO et al. 2011; LAY et al. 2011a). Owing to the small dip angle, such large slip values caused very large uplift of the seafloor, likely

reaching well over 10 m in a large central area of the tsunami source (Fig. 1).

1.1. Modeling of the Tohoku-Oki Tsunami

Early forecasts of the Tohoku tsunami far-field impact, such as those issued by NOAA's PTWC, were not based on realtime tsunami modeling, but instead on the SIFT (Short-term Inundation Forecast for Tsunamis) database; i.e., these were developed through a tsunami data inversion technique and site-specific inundation forecasts (GICA et al. 2008). The SIFT database is a library of tsunami events (referred to as "unit sources"), which were precomputed using a propagation model, for a series of design earthquakes distributed along all the active faults (GICA et al. 2007), each 100 by 50 km in size and with a moment magnitude of $M_w = 7.5$. For a specific event, the inversion uses the SIFT unit sources whose locations and predefined parameters (i.e., dip and rake-angles, slip, depth of source) are closest to the earthquake epicenter and characteristics, adjusted for the observed moment magnitude (GICA et al. 2008). Realtime tsunami elevation data measured by the deep water DART buoys network are used in the inversion to weigh these approximate sources, by constraining the predicted combined elevations to closely agree with DART measurements. These calibrated tsunami events are then used to provide rapid predictions of far-field impact.

Realtime tsunami forecasting in the near-field is more site specific and, hence, is much more difficult to perform and thus less developed. After the event, TSUSHIMA et al. (2011) inverted the offshore wave data from various tsunami wave buoys, recorded 5–10 min before the tsunami reached the coastal tide gauges nearest to the earthquake source, and estimated the distribution of the initial offshore sea surface elevation. They then combined tsunami waveforms from this estimated source to forecast the waves' arrival times and amplitudes at coastal tide gauges. Results agreed sufficiently well with observations to indicate that such a forecasting method could contribute to reliable near-field tsunami warnings. Somewhat more detailed and comprehensive is the approach of FUJII et al. (2011), who estimated a tsunami source for the event by inverting

tsunami waveforms recorded at tide and wave gauges, GPS wave gauges, and deep water DART buoys. The initial seismic parameters were determined from the USGS W-phase moment tensor solution (e.g., strike, dip, slip angle), but the initial wave elevation was based on models of individual subfaults, which were then used to estimate the slip over the total fault, using a least-squares method.

Detailed modeling of the event, both earthquake and tsunami generation, and of tsunami propagation and near- and far-field impacts, which is the object of the present work, is a more involved and lengthy process that was tackled by several groups in the months following the event. Such modeling can help to improve understanding and better explain the processes that led to the triggering of such large waves and caused widespread coastal destruction; and hopefully allow better preparation for future similar events, in terms of mitigation and forecast. Such work first involves developing a relevant tsunami source that accounts for local geological and tectonic processes (i.e., the Japan trench and subduction zone structures), as well as observed seismic (i.e., inverted seismic waves from seismograph measurements) and geodetic (i.e., directly measured seafloor and land deformation) data. Using such a source together with sufficiently accurate and resolved bathymetric and topographic data, numerical models of tsunami generation, propagation, and coastal impact can then be run, whose results are compared to available field data (e.g., tide gauge and deep water DART buoys, runup and inundation measurements). Modeling refinements follow and, once a reasonable agreement between simulations and observations is achieved, numerical results can be used to better understand tsunami processes that unfolded during the event, such as explaining the failures of coastal protection structures. Improved design and construction methods for tsunami mitigation techniques can finally be suggested. Along this line, for instance, YAMAZAKI et al. (2011b, 2012) studied the effects of the Tohoku tsunami on Hawaii, using two of the early proposed finite-source models obtained from seismic and geodetic inversions (LAY et al. 2011a, b), and applying their "Non-hydrostatic Evolution of Ocean Wave" (NEOWAVE) tsunami propagation model (YAMAZAKI et al. 2009). They used

forward modeling of tsunami records at the four DART buoys located nearest to Japan to refine the location of the main fault slip. They then modeled far-field tsunami propagation and compared model results to DART buoy measurements made throughout the Pacific, to GPS buoy and wave gauge data near the Japanese coast, and to tide gauge and runup measurements in Hawaii. They reported a reasonable agreement at most locations between simulations and observations, although they needed to introduce a time shift in the computed time series at the farthest distant locations.

1.2. Modeling of the Tohoku-Oki Earthquake Source

Since the occurrence of the Tohoku event, a large variety of seismic models of the earthquake have been proposed. These were usually based on inverting seismic and/or geodetic data, using the OKADA (1985) model, which assumes a superposition of planar dislocations (i.e., finite faults) embedded in homogeneous elastic half-spaces (HEHS), or a similarly idealized source model of the subduction zone (e.g., DZIEWONSKI and ANDERSON's (1981) spherical layered PREM seismological model; see, e.g., AMMON et al. 2011; Geospatial Information Authority of Japan, 2011; KOPER et al. 2011; PARARAS-CARAYANNIS 2011; POLLITZ et al. 2011; OZAWA et al. 2011; SHAO et al. 2011). One of these seismic inversion sources, referred to as UCSB (SHAO et al. 2011), will be used in this study.

In the present work, to better account for the actual geometry of the Japan trench and its forearc, as well as inhomogeneities in material properties in the subduction zone (e.g., weaker forearc and stiffer subducting plate materials), we developed and used our own source, based on a more comprehensive and detailed Finite Element Modeling (FEM) (MASTERLARK 2003) of the subduction zone near Japan. An earlier implementation of this approach was successfully applied to the 2004 M9 Sumatra-Andaman earthquake (MASTERLARK and HUGHES 2008). This new tsunami source (referred to as University of Alabama; UA), which is detailed later, was developed by inverting onshore and offshore geodetic data (similar to other sources listed above) but, rather than using Okada's idealized HEHS solution, we used 3D

FEMs that simulate elastic dislocations along the plate boundary interface separating the stiff subducting Pacific Plate from the relatively weak forearc and volcanic arc of the overriding Eurasian plate.

Another aspect of tsunami sources that may significantly affect the accuracy of simulations in a propagation model is whether one assumes that the maximum seafloor deformation is triggered at once in the model for the entire source area, or that subareas of the source are triggered as a time sequence that mimics the actual earthquake event. Such a time sequence can be obtained as a result of seismic inversion methods. For tsunamis that are only triggered over a relatively small source area (such as for Tohoku 2011), it has been customary to assume that the source can be triggered at once. However, it appears from seismic inversion results of this event (e.g., Harvard CMT) that the main event lasted for 3–4 min, during which tsunami waves may have propagated a large distance onshore. Hence, in the present case, it may be important to consider this timing effect and resolve the wave interferences (constructive or destructive) that may have resulted. The sensitivity of tsunami simulations to this timing aspect will be presented later in this work. Additionally, we will study the sensitivity of results to the way the tsunami is initially specified in the propagation model: (i) either as a free surface elevation with no initial velocity (as it is customary to do in most studies owing to the near incompressibility of water and small rise times); (ii) or as a more realistic time-dependent bottom boundary condition (in this case a different type of model, NHWAVE, that allows for such a boundary condition to be specified on the seafloor as a function of space and time, will first be used during 300 s, before moving results into a long wave propagation model; this is detailed later).

1.3. Tsunami Generation and Propagation Models

Large coseismic tsunamis have usually been simulated using numerical models based on the nondispersive (i.e., hydrostatic) Nonlinear Shallow Water (NSW) wave equations (e.g., KOWALIK and MURTY 1993; SATAKE 1995). By contrast, since the late 1990s, our research group has pioneered the use of fully nonlinear and dispersive (i.e.,

non-hydrostatic) Boussinesq models (BM), with extended dispersion properties. These were initially applied to the simulation of landslide tsunamis, in which dispersive effects are important owing to the shorter wavelengths (WATTS et al. 2003; DAY et al. 2005; TAPPIN et al. 2008; ABADIE et al. 2012), but more recently also to the simulation of coseismic tsunamis (GRILLI et al. 2007, 2010; IOUALALEN et al. 2007; KARLSSON et al. 2009). Although dispersive effects may not always be significant in long tsunami wave trains, when they are called for, BM equations feature the more extended physics required to simulate such effects. IOUALALEN et al. (2007), for instance, showed differences in the computed elevation of leading waves for the 2004 Indian Ocean tsunami event near Thailand, of up to 30 % when simulating the tsunami using a BM with or without the dispersive terms (i.e., in NSW mode in the latter case). The BM model used in this work, FUNWAVE, was initially developed and validated for coastal wave dynamics problems (WEI et al. 1995; CHEN et al. 2000, 2003; KENNEDY et al. 2000); later, however, FUNWAVE was used to perform many successful tsunami case studies, as discussed above. In its most recent implementation, the FUNWAVE-TVD code in Cartesian (SHI et al. 2012) or spherical coordinates with Coriolis effects (KIRBY et al. 2009, 2012) (note, the latter implementation is currently only weakly nonlinear) uses a Total Variation Diminishing (TVD) shock-capturing algorithm to more accurately simulate wave breaking and inundation. The code is fully parallelized using the Message Passing Interface (MPI) protocol. Because of their more complex equations, BMs are typically more computationally demanding than NSW models. However, the optimized MPI implementation of FUNWAVE-TVD has highly scalable algorithms, with a typical acceleration of computations of more than 90 % the number of cores in a computer cluster (SHI et al. 2012). Hence, running such models over large ocean basin-scale grids with sufficiently fine resolution is no longer problematic.

In the present study, FUNWAVE-TVD is used in its Cartesian implementation to simulate the near-field tsunami propagation from the source to the Japan coast and in its spherical implementation to simulate the far-field tsunami propagation from the source to distant locations in the Pacific Ocean. Results will show that dispersive effects do not appear to be very significant in the near-field for the type of tsunami sources used to date for Tohoku 2011 (i.e., purely coseismic). However, as these sources are refined (both in space and time) to include more complex geological and seafloor processes (e.g., sub-faults, splay faults, submarine mass failure), one will increasingly have to model the superposition and interactions of shorter and hence more dispersive waves, which requires using models that simulate this type of physics (such as BMs). Additionally, although in the present work we will not use a fine enough coastal grid resolution for such phenomena to appear in simulation results, recent work showed that even very long waves may transform into undular bores over a wide shelf as they approach the shore (MADSEN et al. 2008; KIM and LYNETT 2011). Such bores are made of a large number of short waves (with periods more akin to very long swells), which are thus highly dispersive, overlying a longer surge that may enhance tsunami coastal impact. Nondispersive NSW models cannot simulate such processes (KIM and LYNETT 2011).

In the following, we first present in Sect. 2 the field data used in the comparisons with model results. We then present in Sect. 3 the definition and development of the tsunami sources used as initial conditions in the propagation models. In Sect. 4, we briefly summarize the propagation model equations and features and discuss model setup. Results are finally presented and discussed in Sect. 5. Specifically, we report on simulations of the far- and near-field coastal impact of the Tohoku tsunami, using FUNWAVE-TVD. The model is initialized with either the USCB or the new UA source. Results are compared with measurements of surface elevations at DART and tide gauge buoys, and runup and inundation heights on the shore. Computations are performed in a series of nested model grids, with varying resolution (down to 250 m nearshore) and sizes. Some cases are run with or without dispersion terms in the BM equations, to assess effects on results of the latter. Additionally, as indicated before, we also study the sensitivity of model results to the type of initialization.

2. Field Data

Many field measurements of the tsunami were made both during and after the event, which primarily consisted of: (i) deep water DART buoy measurements of surface elevation (Lay et al. 2011b); (ii) nearshore GPS buoy or tide gauge measurements of surface elevation (Yamazaki et al. 2011a); and (iii) onshore field surveys of runup and inundation height (Mori et al. 2011, 2012). These recorded data and post-event surveys, which were conducted by a large international team of scientists along a 2,000 km stretch of the Japanese coast at more than 5,300 individual locations, generated the largest tsunami survey dataset ever produced (Mori et al. 2011, 2012).

2.1. DART Buoys

Offshore, tsunami measurements from the DART network are critical elements in (near) realtime tsunami forecasting and modeling (Titov et al. 2005). There are 39 operational DART buoys installed and operational throughout the Pacific and Atlantic oceans, whose measurements can be obtained on the internet as soon as they are available (http://www.ndbc.noaa.gov/dart.shtml). At each buoy, data is routinely collected in 15 s to 15 min intervals, depending on the level of alert. When the passage of a tsunami has been identified at a particular buoy (after the DART network has been put on alert), average surface elevation data is transmitted every 15 s during the initial few minutes, followed by 60 s intervals (Gonzalez et al. 1998). To obtain the tsunami signal, this data first needs to be filtered to remove the tidal signal. In this study, we analyzed data from the 18 DART buoys which were located in the path of the tsunami (Lay et al. 2011b), and used it for comparison with model results obtained at the same locations (Fig. 3). Here, DART data was detided using a Butterworth filter and then interpolated to get equal intervals of 15 s.

2.2. GPS Buoys

Near the Japanese coastline, a series of moored GPS-mounted buoys from the NOWPHAS (Nationwide Ocean Wave information network for Ports and HArbourS; http://nowphas.mlit.go.jp/index_eng.html) are moored in water depth of 100–300 m and at a distance of 10–20 km from the coastline (Figs. 1, 3). These sturdy buoys resisted the large tsunami waves during the Tohoku 2011 event and provided time series of surface elevation, through the measurement of their 3D position every one second (using RTK-GPS technology to position the GPS mounted on top of each buoy). Tsunami elevation was obtained by a low-pass filtering, with a moving average technique (Kato et al. 2005).

2.3. Runup and Inundation Field Measurements

Field surveys started two days after the tsunami and were conducted by several research groups totaling 299 scientists from 64 different universities/institutes (Mori et al. 2011, 2012). Inundation (local tsunami height above sea level) and runup heights (elevation at maximum inundation) were measured at a total of 5,247 points (see Fig. 17 central panel). Inundation heights were obtained from watermarks on trees, walls, and buildings, and detided for the time of tsunami impact. Runup heights were derived from the maximum extent of debris deposits and water marks.

2.4. Bathymetric and Topographic Data

Bathymetric and topographic data were obtained and compounded from several sources. These include: the 1 arc-minute resolution ETOPO1 database (Amante and Eakins 2009); the 500 m resolution J-EGG500 bathymetry (JODC-Expert Grid data for Geography) along the Japanese coastline and the 1 arc-second ASTER topographic data (Advanced Space-Borne Thermal Emission and Reflection Radiometer; Yamaguchi et al. 1998). Although Digital Elevation Models (DEMs) have already been developed for this area (e.g., the GMRT of Ryan et al. 2009), which compile available topography datasets into grids useful for computational models, early tests showed that these DEMs do not provide a smooth topography along the Japanese coastline, which is problematic for simulating coastal impact of tsunamis in propagation models.
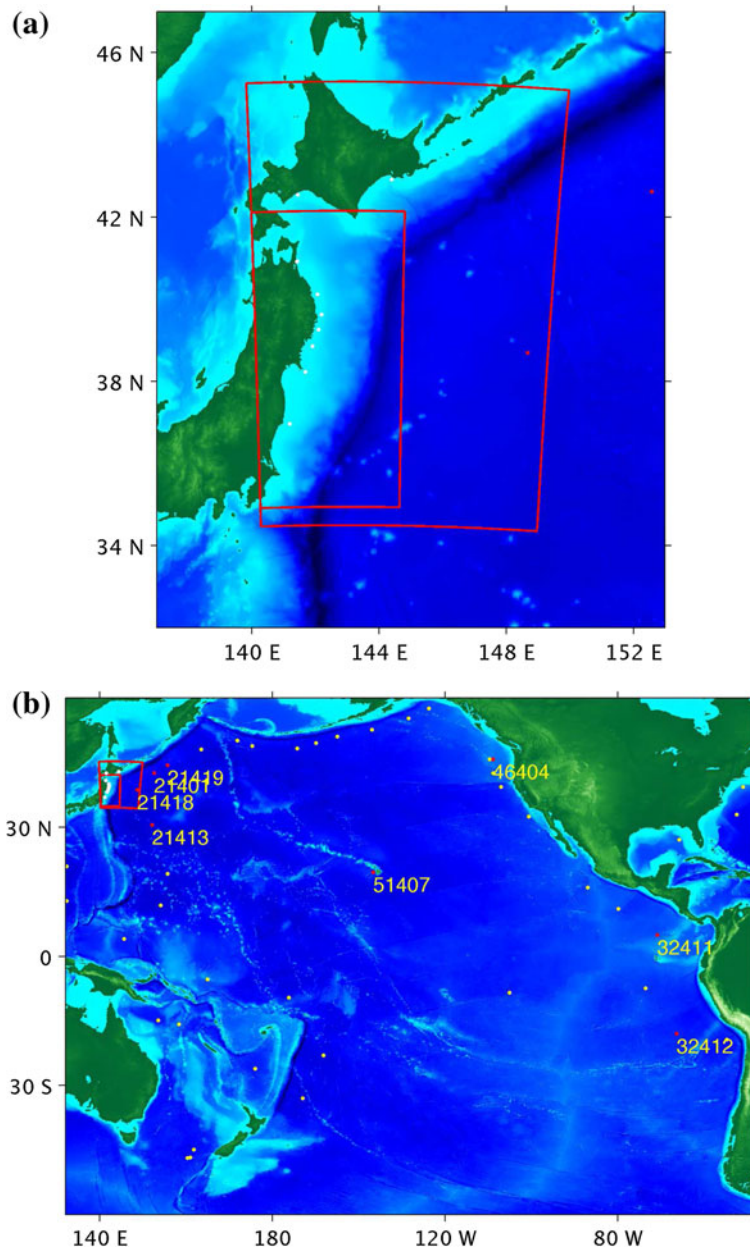
Figure 3
Computational domains for: **a** near-field (regional) simulations with FUNWAVE-TVD (Cartesian grid) and NHWAVE; **b** far-field (Pacific basin scale) simulations with FUNWAVE-TVD (4′ spherical grid), with the marked location of 18 DART buoys (*yellow dots* not used; labeled *red dots* used in comparisons). The smaller and larger *red boxes* mark the boundaries of the coastal 250 m, and regional 1,000 m, resolution grids, respectively (Table 1). The *white dots* in panel (**a**) indicate the location of the GPS buoys of Fig. 11

For the coarser computational grids, which are used to model the tsunami distant propagation across the Pacific Ocean, or for our initial 1 km resolution simulations near the tsunami source, the grid bathymetry was only generated based on ETOPO1 data. For higher resolution grids, such as used nearshore (e.g., 250 m), we interpolated both the ASTER topography and the JODC bathymetry to our computational grid (using a linear interpolation method). For points, which are in the ocean (i.e.,

where the ASTER topographic height is zero), the depth was found by interpolating between all other points (i.e., the final result is a linear interpolation of ASTER and JODC data onto the computational grid). The most substantial problem with this approach is that, in narrow bays where no bathymetric measurements are available from the JODC data, depth is set to zero in the entire area, most likely causing an underprediction of tsunami runup in such cases (such as along the Sanriku/Ria coast; see Sect. 5).

3. Source Model and Initial Conditions

As discussed in the introduction, the traditional approach to initializing a long wave propagation model for coseismic tsunami simulations is based on the OKADA (1985) solution, which provides the seafloor deformation due to the motion (slip) of a fault in an elastic homogeneous half-space. In the latter, the dip angle is defined as the angle between the fault and a horizontal plane (between 0° and 90°); the strike angle is the fault direction relative to north (0° to 360°; defined such that the fault dips to the right of this angle); and the rake is the direction the hanging wall moves, measured relative to the fault strike (–180° to 180°). In finite fault source models, such as USGS's (Fig. 1), which are obtained by seismic inversion (i.e., using seismic waves measured at many seismographs around the earth, together with a model of the Earth's crust), Okada's solution is applied to many subfaults on the basis of the inverted slip distribution (and other parameters). Many inverted slip distributions have been published since the event, which were discussed in the introduction. Among those, we found that the source referred to as UCSB (SHAO et al. 2011) provided the best agreement with tsunami measurements. [To reach this conclusion, we simulated two preliminary UCSB sources as well as both a preliminary and a final USGS source].

As discussed in the introduction, to better account for the actual geometry of the Japan trench and its forearc, as well as inhomogeneities in material properties in the subduction zone, we also developed and used our own source, referred to as University of Alabama (UA) source. The UA source is based on a detailed Finite Element Modeling (FEM) of the subduction zone near Japan, in which onshore and offshore geodetic data measured during the event are assimilated as part of the solution. While still not perfect, as we shall see, this source produces significant shallow slip, several tens of meters along the updip portion of the rupture near the trench (likely due to the simulated weak forearc material), which allows better simulating some of the tsunami observed features and impact. In the following, we present and compare results of tsunami generation, propagation, and impact for the UCSB and UA sources.

3.1. UCSB Source

The source we denote as UCSB is based on the slip history derived by SHAO et al. (2011) using teleseismic body and surface seismic waves. The UCSB source assumes the earthquake epicenter was located at 38.10°N and 142.86°E, and the seismic moment was $M_o = 5.84 \times 10^{22}$ Nm, for a dip angle of 10° and a strike angle of 198°. Figure 4 shows the maximum slip distribution obtained for this source, as well as the corresponding maximum seafloor uplift (note, for comparison with uplift predicted by the UA source, the UCSB uplift is replotted in Fig. 7d at the same scale and compared to field measurements). For the time-dependent triggering of this source, the rise-time computations are based on an asymmetric cosine parameterization, described by JI et al. (2002). As we shall see, the time-dependent triggering of this source in FUNWAVE results in somewhat different wave elevations at the end of the earthquake main shock, as compared to the instantaneous triggering of the entire source.

3.2. UA Source

As discussed above, this source (referred to as UA; Figs. 5, 6, 7) is developed by simulating the deformation of the M9 2011 Tohoku earthquake using FEMs of the subduction zone, rather than idealized semi-analytical solutions (e.g., Okada). These FEMs, which simulate an assembly of dislocation surfaces embedded in a 3D elastic domain, are constructed with ABAQUS (2009) and share the general geometry, mesh, and distribution of material
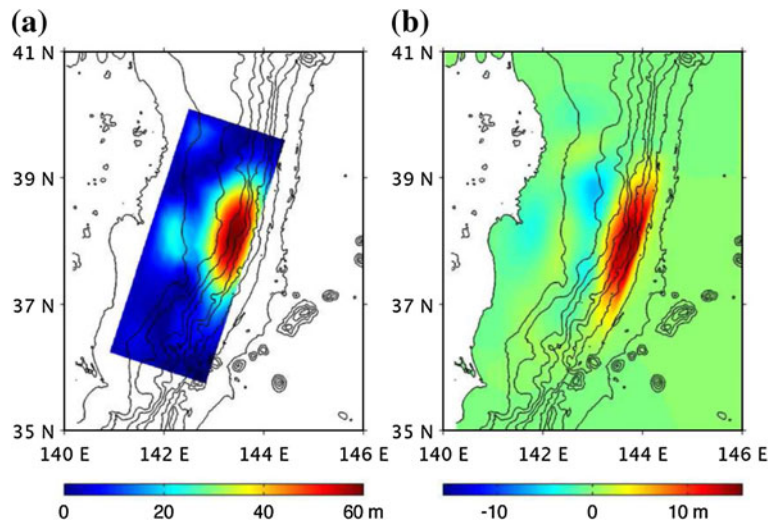
Figure 4
UCSB source (SHAO et al. 2011): **a** Source area and maximum slip distribution; **b** vertical seafloor displacement

properties of FEMs presented by MASTERLARK and HUGHES (2008, 2010). The domain is partitioned into six regions representing the different elastic properties of the forearc, volcanic arc, shallow and deep backarc, oceanic crust, and mantle (Fig. 5). An innovational aspect of this model is its ability to simulate dislocation along a dipping fault having relatively weak materials of the overriding plate juxtaposed across the fault from relatively stiff oceanic crust of the downgoing slab (MASTERLARK and HUGHES 2008).

The FEM domain is configured to simulate net deformation along a rupture surface having the along-strike curvature of the Japan Trench and a dip of about 12°. The dimensions of the curved rupture are about 750×200 km along-strike and downdip, respectively. This rupture surface is partitioned into 98 dislocation patches. The distribution of slip along the rupture is calibrated via least-squares inverse methods, by assimilating three-component geodetic data from 521 onshore GPS stations (GEONET of Japan, processed by the ARIA team at JPL/Caltech; ftp://sideshow.jpl.nasa.gov/pub/usrs/ARIA) and 5 offshore stations (SATO et al. 2011) that characterize the near-field coseismic deformation of the M9 Tohoku earthquake.

The forward model for deformation caused by a distribution of dislocation patches, scaled to account for the relative data uncertainties and regularized with Laplacian smoothing is:

$$[\mathbf{G}_w + \beta \mathbf{L}]\mathbf{m} = \mathbf{d}_w \qquad (1)$$

where $\mathbf{G}_w = \mathbf{WG}$ and $\mathbf{d}_w = \mathbf{Wd}, \mathbf{G}$ is a matrix of Green's functions for displacement due to dislocation for both thrust and strike-slip components, $\mathbf{m}$ is a column vector of dislocation parameters, $\mathbf{d}$ is a column vector of displacement observations, $\mathbf{W}$ is a diagonal matrix, where diagonal elements correspond to the relative data uncertainties, and $\mathbf{L}$ is a matrix of coefficients that satisfies $\mathbf{Lm} \approx \nabla^2 \mathbf{m} = 0$ for a given set of boundary conditions. The boundary conditions for the Laplacian smoothing are zero slip along the northern, southern, and downdip edges of the rupture. The trench-normal slip gradient is zero along the updip boundary, which follows the trace of the Japan Trench (Fig. 7). The Green's functions are calculated with the FEMs using the method of kinematic constraint equations (MASTERLARK 2003) and undrained elastic parameters (WANG 2000).

We sweep through damping coefficients, β, and determine a suite of corresponding least-squares solutions for $\mathbf{m}$ by inverting the forward model. The damping coefficient controls the trade-off between fitting the data and having a smooth solution. We then calculate the weighted least-squares misfit ($\mathbf{e}^T\mathbf{e}$), where $\mathbf{e}$ is the prediction error $\mathbf{e} = \mathbf{d}_w - \mathbf{G}_w \mathbf{m}$ and
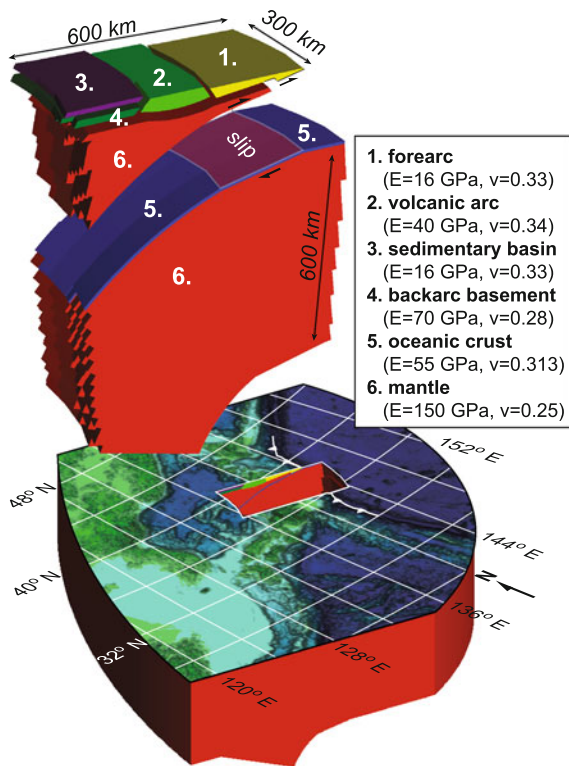
Figure 5

FEM domain and configuration. The domain is partitioned to include a characteristic distribution of elastic properties for the subduction zone according to HUGHES *et al.* (2010). A portion of the near-field region is shown in exploded view to reveal the structure and configuration of materials. Material properties of the mantle and crust are drained and undrained, respectively. The juxtaposition of weak and strong materials across the dipping fault is fundamental to the subduction zone structure and strongly influences deformation predictions. The rupture is simulated with elastic dislocations along the dipping surface separating the stiff subducting slab and weak overriding plate. This downdip interface between the two plates is welded. The *top* of the domain is a stress-free surface and the lateral and basal boundaries are zero displacement. The initial conditions are equilibrium. The coseismic slip is calibrated to onshore and offshore geodetic data, using least-squares inverse methods and FEM-generated Green's functions

T is the transpose operator, as a function of regularized solution length $(\mathbf{Lm})^T(\mathbf{Lm})$. The solution that corresponds to the knee of the curve plotted as the logarithm of $\mathbf{e}^T\mathbf{e}$ versus the logarithm of $(\mathbf{Lm})^T(\mathbf{Lm})$ provides a good compromise between fitting the data and smoothing (ASTER *et al.* 2005; Fig. 6). This is our preferred solution. The maximum magnitude of slip for this solution is about 51 m, and the solution corresponds to a moment magnitude of $M_w = 8.8$, which is perhaps slightly on the lower side. For this
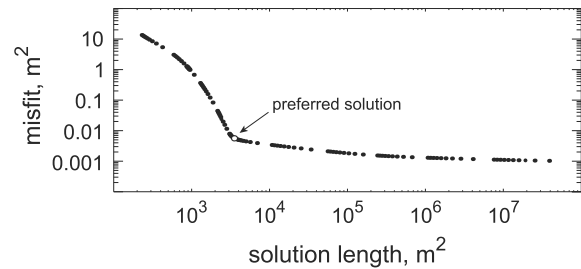

Figure 6

L-curve. Each *black circle* represents the solution length versus misfit associated with a given damping coefficient β. The knee of the L-curve is the preferred solution, which is a compromise between fitting the data versus satisfying the smoothing constraints (ASTER *et al.* 2005)

reason, we also investigated an alternative solution that corresponds to a moment magnitude of $M_w = 9.0$ (in better agreement with seismogenic studies of the event) by reducing the damping coefficient, which relaxes the smoothing constraints and consequently improves the fit to the data. The maximum slip magnitude for this alternative solution is 85 m. Predictions of geodetic data are excellent for both models. The slip distributions and predictions are illustrated in Fig. 7. Finally, the time sequence information necessary to perform the time triggering of this source in the tsunami propagation models is obtained from the GPS inversion performed by YUE and LAY (2011), and Fig. 8 shows the resulting combination of the UA source uplift shown in Fig. 7c and this time sequence.

4. Hydrodynamic Models

This study makes use of three closely related numerical models; spherical- and Cartesian-coordinate versions of the Boussinesq-type model FUNWAVE-TVD (SHI *et al.* 2012; KIRBY *et al.* 2012), and the nonhydrostatic model NHWAVE (MA *et al.* 2012). NHWAVE is used here to specify a time-dependent source for tsunami generation triggered by the transient motion of the seafloor, which is not a feature of FUNWAVE-TVD. FUNWAVE-TVD is used in its spherical coordinate form to model tsunami propagation over ocean-scale distances, while the Cartesian version is used to model local response and inundation in Japan's coastal regions. A brief
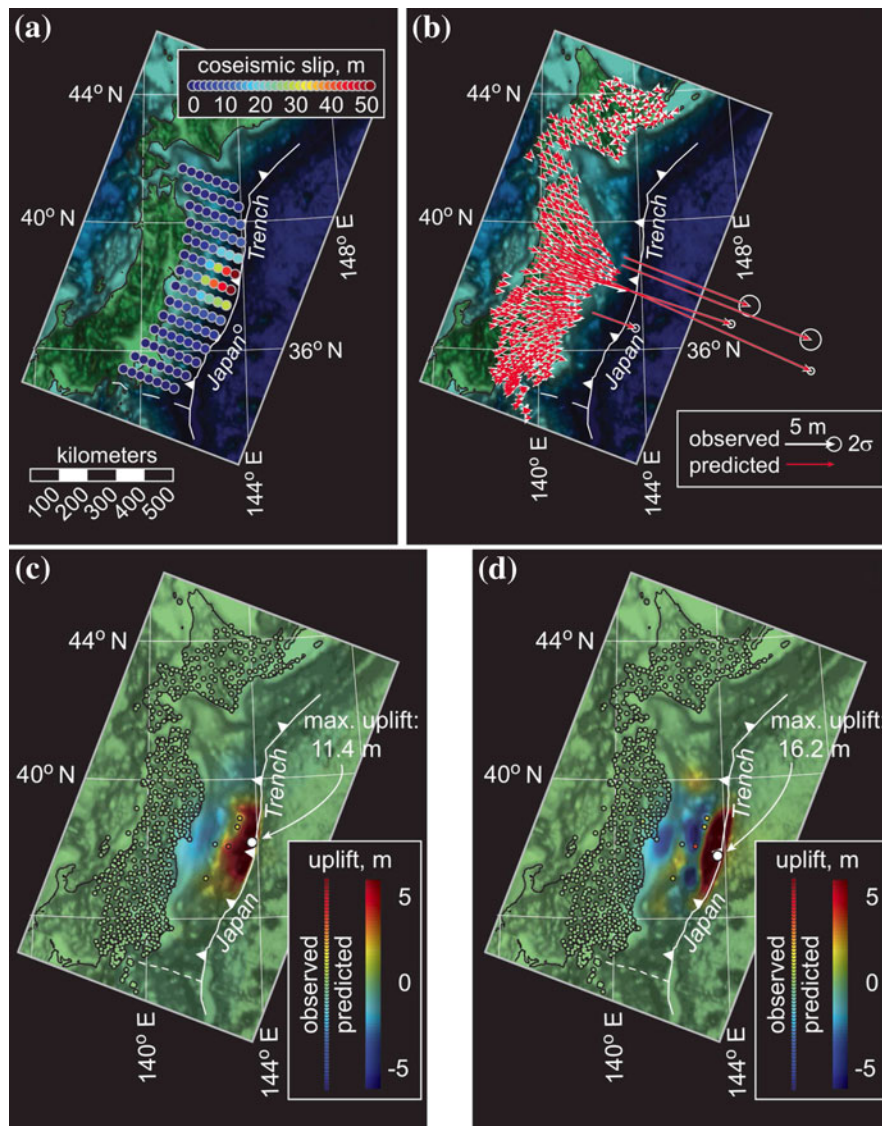
Figure 7

FEM-based coseismic slip and deformation. **a** Coseismic slip distribution (M8.8 UA source). The position of each *circle* represents the surface projection of the centroid for a slip patch, each of which comprises four note pairs that simulate elastic dislocation with kinematic constraint equations (MASTERLARK and HUGHES 2008). The coseismic slip is concentrated near the trench, with a maximum magnitude of 51 m. Both *horizontal* (**b**) and *vertical* (**c**) deformation are well predicted by the FEM. *Vertical* seafloor motions for UCSB source (**d**) poorly predict seafloor geodetic data (SATO *et al.* 2011) and, in particular, predict that the main transition from subsidence to uplift is several tens of kilometers closer to the trench than is indicated by the offshore geodetic data

overview of each model is provided here; readers are referred to the primary citations for further details.

Results of FUNWAVE-TVD simulations of the Tohoku 2011 tsunami are presented in the next section, based on different initial conditions and model setups. We compute the tsunami far-field propagation in the domain shown in Fig. 3 and compare results

with measurements at some of the DART buoys also shown on the figure. Near-field tsunami impact is computed in a smaller, but more finely resolved, regional domain encompassing both the earthquake source and the Japan coastline (see also Fig. 3) and results are compared with measurements made at coastal GPS buoys and runup/inundation data
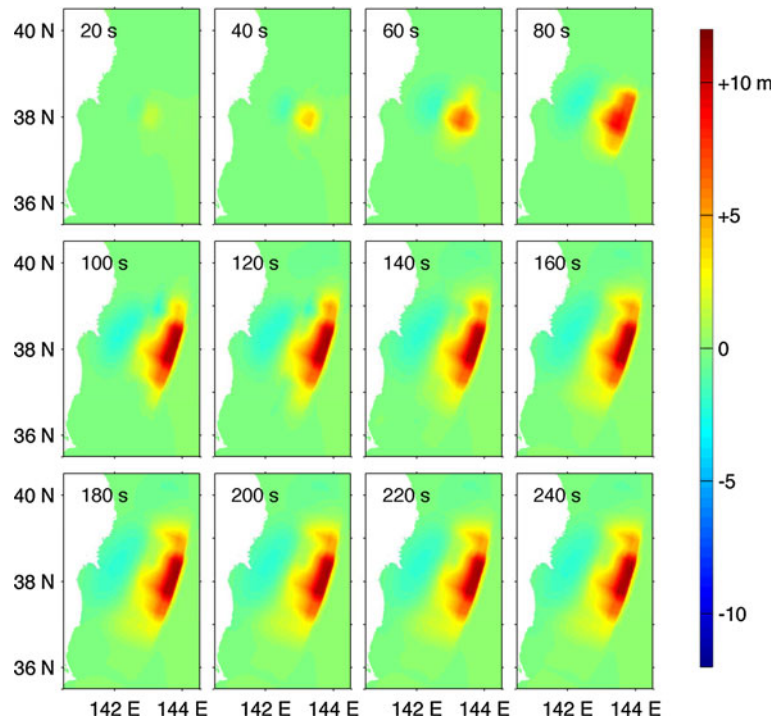
Figure 8
Snapshots of cumulative seafloor uplift caused by the UA source (Fig. 7c), as a function of time, in 20 s intervals. The timing sequence is obtained from YUE and LAY (2011)

obtained from field surveys. For both domains, sponge layers are specified along open boundaries, which are sufficiently wide to absorb outgoing waves and hence nearly eliminate wave reflection from the domain boundaries.

4.1. Horizontal Model Structure

Both FUNWAVE-TVD and NHWAVE make use of a finite-volume TVD scheme, using a well-balanced scheme for the pressure gradient following LIANG and MARCHE (2009). This scheme is used to represent basic local and advective accelerations and pressure gradient effects. The scheme is mass conserving and handles shock tracking and moving boundary effects accurately and efficiently. Both models are parallelized using a horizontal domain decomposition, and the parallelization is implemented using the MPI protocol. Both models utilize a third-order Strong Stability Preserving (SSP) Runge-Kutta scheme (GOTTLIEB *et al.* 2001) for

forward marching in time, with adaptive time-stepping based on flow conditions.

4.2. Cartesian FUNWAVE-TVD

The Cartesian-coordinate version of FUNWAVE-TVD, described by SHI *et al.* (2012), solves the fully nonlinear and weakly dispersive Boussinesq equations of WEI and KIRBY (1995), extended to include provisions for a time-dependent reference elevation (KENNEDY *et al.* 2001) and correct potential vorticity conservation to the order of approximation in the velocity field structure (CHEN 2006). Following earlier work by ERDURAN *et al.* (2005) and TONELLI and PETTI (2009), the code employs a hybrid numerical scheme, which uses a MUSCL-TVD finite volume formulation for the underlying NSW equations (YAMAMOTO *et al.* 1998; ERDURAN *et al.* 2005), together with a finite difference treatment of higher-order dispersive terms representing the effects due to deviation from hydrostatic pressure conditions.

During simulations, when the local surface elevation to depth ratio exceeds 0.8, wave breaking is assumed to occur and the model Boussinesq equations are switched to the NSW equations by turning off dispersive terms. Earlier work shows that with this method, the TVD front tracking algorithm in the model and related numerical diffusion yield accurate representations of wave height decay in the surfzone (SHI *et al.* 2012). FUNWAVE-TVD has been validated against a large set of analytical, laboratory, and field tsunami benchmarks (TEHRANIRAD *et al.* 2011) as part of the development of tsunami hazard maps for the East Coast of the USA (see also ABADIE *et al.* (2012) for a recent application).

4.3. Spherical FUNWAVE-TVD

The spherical-coordinate version of FUNWAVE-TVD, described by KIRBY *et al.* (2009, 2012), solves weakly nonlinear and dispersive Boussinesq equations on a rotating sphere. The governing equations are put in conservative, well-balanced form and implemented using the same numerical approach as used for the Cartesian version of the code (SHI *et al.* 2012). KIRBY *et al.* (2012) describe the parallelization of the resulting model and perform a parametric test of the importance to tsunami evolution of both dispersive and Coriolis effects resulting from a range of relative tsunami source width in the main propagation direction.

4.4. NHWAVE

The nonhydrostatic wave model NHWAVE, developed by MA *et al.* (2012), provides a numerical solution of the three-dimensional Navier Stokes equations for incompressible flow, but with the simplifying assumption of a single-valued water surface displacement. The model uses a second-order Godunov-type TVD method (ZHOU *et al.* 2001; LIANG and MARCHE 2009) for horizontal gridding, applied on multiple vertical levels defined by a standard bottom- and surface-following σ-coordinate formulation. The effect of a time-dependent moving bottom is implemented in the model, which may thus be used to simulate the transient nature of tsunami sources due to both coseismic and submarine mass failure (SMF) events. MA *et al.* (2012) have validated the SMF aspect of the model performance in comparison to laboratory data for highly dispersive conditions presented by ENET and GRILLI (2007). The model uses the package HYPRE (2006) to solve the resulting pressure Poisson equation. The present model application assumes perfect fluid conditions. Solutions of the resulting numerical implementation of the Euler equations are usually accurately obtained using only three to five vertical σ levels, as shown in MA *et al.* (2012).

5. Results

We simulate the propagation of the Tohoku 2011 tsunami across the Pacific Ocean, as well as its coastal transformations, runup, and inundation along the Japanese coastline, in a series of computational domains (Table 1). To correct for Earth's sphericity in models that use Cartesian coordinates, a transverse secant Mercator projection is used (similar to the UTM system), with its origin located at (39°N, 143°E). This transformation leads to small grid distortions, which are deemed negligible.

In all simulations, free-slip (wall) boundary conditions are applied on the lateral boundaries of the

Table 1

Grid sizes and resolutions, and sources of bathymetry, for the Tohoku 2011 simulations with NHWAVE or FUNWAVE-TVD (Cartesian or spherical). See Fig. 3

Grid/model	Size	Resolution	Bathymetry
Regional/NHWAVE	(−250, 250) km; (−400, 400) km	1 km	ETOPO1 (1′ arc)
Regional/FUNWAVE	(−250, 550) km; (−500, 700) km	1 km	ETOPO1 (1′ arc)
Pacific/FUNWAVE	(132°E, 68°W); (60°S, 60°N)	4′ arc	ETOPO1 (1′ arc)
Coastal/FUNWAVE	(−250, 150) km; (−450, 350) km	250 m	JODC (500 m)/ASTER (3″ arc)

computational domains. To prevent nonphysical reflection from these boundaries, sponge layers are specified over a number of grid cells (inside of the outer domain boundary marked in Fig. 3), for which damping terms are activated in the model equations. Specifically, in simulations of tsunami propagation with FUNWAVE over the Pacific grid, sponge layers are 100 km thick along all lateral boundaries. For the NHWAVE and FUNWAVE simulations in the 1,000 m regional grid, sponge layers are 50 km thick in the north and south ends of the domain, and 200 km thick in the east. Finally, for the FUNWAVE simulations in the 250 m coastal grids, sponge layers are 50 km thick along the north, east and south boundaries. Note, in order to avoid the triggering of instabilities due to sharply varying bathymetry during wetting-drying in NHWAVE simulations in the regional grids, the critical depth for wetting-drying is set to 1 m, and the bottom drag coefficient to 0.001. Since NHWAVE is only used to compute the initial tsunami waveform, one does not have to resolve wetting-drying at the coast. In all FUNWAVE-TVD simulations, the minimum depth for the wetting-drying algorithm is set to 1 cm and the bottom drag coefficient to 0.01. Work done while validating the hydrodynamic models for NOAA's National Tsunami Hazard Mitigation Program (NTHMP) mandatory benchmarks (TEHRANIRAD *et al.* 2011) has shown that, for the type of grid resolution used here, nearshore and inundation results are relatively insensitive to the value of the bottom drag coefficient. Higher-resolution inundation mapping, however, where buildings and vegetation can be resolved, would naturally require a more complex parameterization of friction.

All numerical simulations begin with 300 s of computations of the initial tsunami waveform in the 500 by 800 km, 1,000 m resolution, regional grid (Table 1). As discussed before, we first study the sensitivity of results to whether the coseismic tsunami sources are triggered at once or in a time sequence in the propagation model. In the latter case, we also verify whether it is relevant to linearly superimpose nonmoving free surface elevations when triggering large tsunami waves in a time sequence. To assess this effect, we directly specify the seafloor deformation as a time-dependent bottom boundary condition, rather than as a "hot start" initial condition on the

free surface, with no velocity; since one can only specify the initial condition on the free surface in FUNWAVE-TVD, we use NHWAVE to do so. Thus, three types of initializations are tested and compared in the regional grid: either (a) a hot start of FUN-WAVE-TVD, by specifying the maximum seafloor vertical displacement of each coseismic source (e.g., such as in Fig. 4b) over the entire domain at once, as a free surface elevation without initial velocity; or the time-dependent triggering of each coseismic source, (b) directly on the free surface in FUNWAVE without initial velocity, or (c) as a bottom boundary condition in NHWAVE. Results at 300 s (or 5 min) are then interpolated, through a one-way coupling, from the regional grid onto one of two FUNWAVE-TVD grids (Table 1): either (i) directly on the 4' arc spherical grid for far-field transpacific simulations; or (ii) following an additional 10 min of propagation in the 1,000 m FUNWAVE grid, onto the 250 m resolution coastal Cartesian grid (in order to both get the westward propagating waves to fully enter the 250 m grid and separate these from the eastward propagating wave), to perform all near-field simulations. The latter include computations of time series at GPS tide buoys as well as computations of runup and inundation along the coast.

5.1. *Result Sensitivity to Initialization Method*

The sensitivity of results to the three source triggering methods was assessed for the UCSB coseismic source shown in Fig. 4. Figures 9 and 10 show the initial free surface elevations at $t = 300$ s and a transect in those, respectively, simulated using the three different initialization methods discussed above. Significant differences can be seen, in both surface elevation and wavelength, between the instantaneous method (a) and the two time-dependent methods (b, c). Smaller differences can then be observed between the latter two methods, with the time-triggering in NHWAVE resulting in slightly reduced maximum (positive or negative) elevations and in waveforms with less higher-frequency oscillations than for the time-triggering in FUNWAVE-TVD. This might be due to the adjustment of the solution kinematics to the nonphysical superposition of free surface increments with no initial velocity.
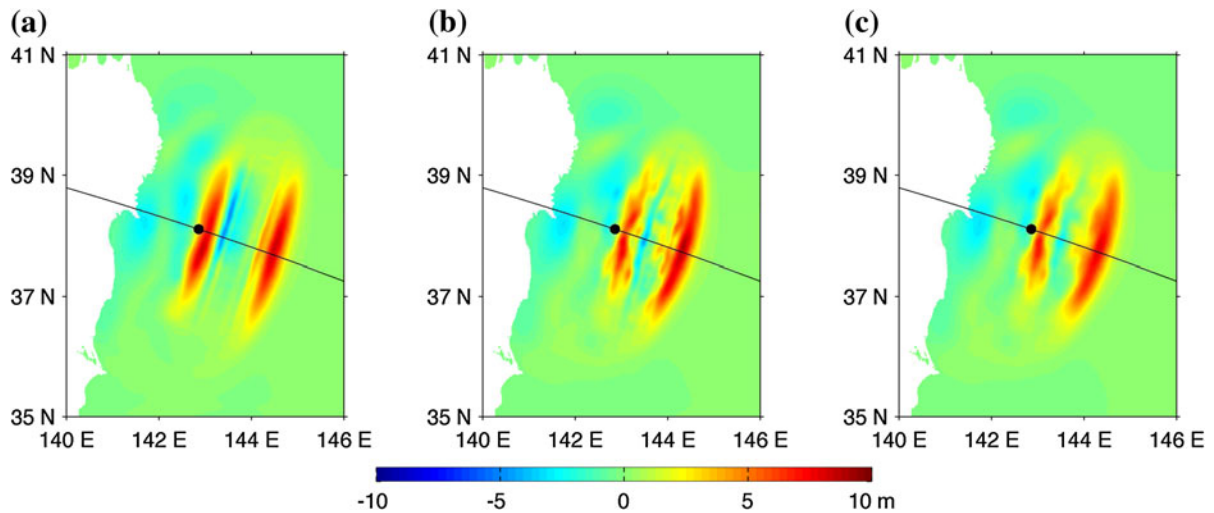
Figure 9
Sensitivity of initial tsunami elevation computed at $t = 300$ s, to the initialization method used, for the UCSB coseismic source: **a** instantaneous triggering on the free surface in FUNWAVE-TVD, using the maximum seafloor uplift; **b** time-varying triggering on the free surface in FUNWAVE-TVD, using the instantaneous seafloor uplift; and **c** time-varying seafloor uplift specified as a boundary condition in NHWAVE (with 3 *vertical σ*-levels). *Black lines* indicate locations of transect used in Fig. 10, and the *black dot* is the origin of the axis in the latter figure
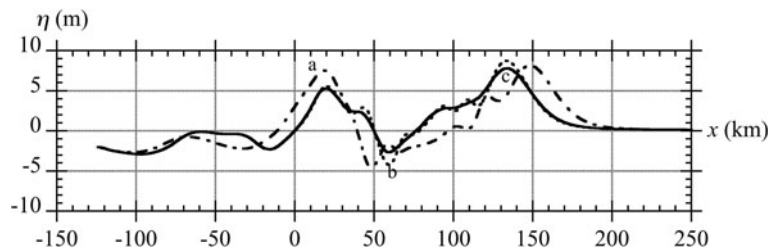
Figure 10
Transects in results of Fig. 9, perpendicular to the fault (at 198°), relative to the JMA hypocenter (38.10N 142.860E), method: (*a*) instantaneous triggering in FUNWAVE (*chained line*); (*b*) time dependent triggering in FUNWAVE (*short broken line*); (*c*) time dependent triggering in NHWAVE (*straight line*). Positive distances refer to distance east, towards the Pacific, and negative distances to distance west, towards the Japanese coastline

Overall, these results justify using triggering method (b), which is more accurate and realistic, to compute the initial tsunami waveform; this will be done in all the following computations for both the UCSB and UA sources. Note, as indicated before for the latter source, the timing information for the time triggering of seafloor uplift patches is obtained from YUE and LAY (2011).

5.2. Surface Elevation at Coastal GPS Buoys

The accuracy of tsunami generation using the UCSB and UA sources is assessed by comparing simulated surface elevations in the regional grid computations against observations made at nine coastal stations equipped with GPS buoys (Fig. 11). After initialization at $t = 300$ s with NHWAVE results (with time-dependent triggering on the seafloor), the Cartesian FUNWAVE-TVD code is run on the 800 by 1,200 km regional grid, with a 1,000 m resolution (Table 1). [Note, results for the M9 UA source are not detailed here as they were found to agree less well with observations than those of the M8.8 UA source; hence, hereafter, the latter source is used and referred to as simply the UA source]. Overall, results of the UA source are found in better agreement with observations
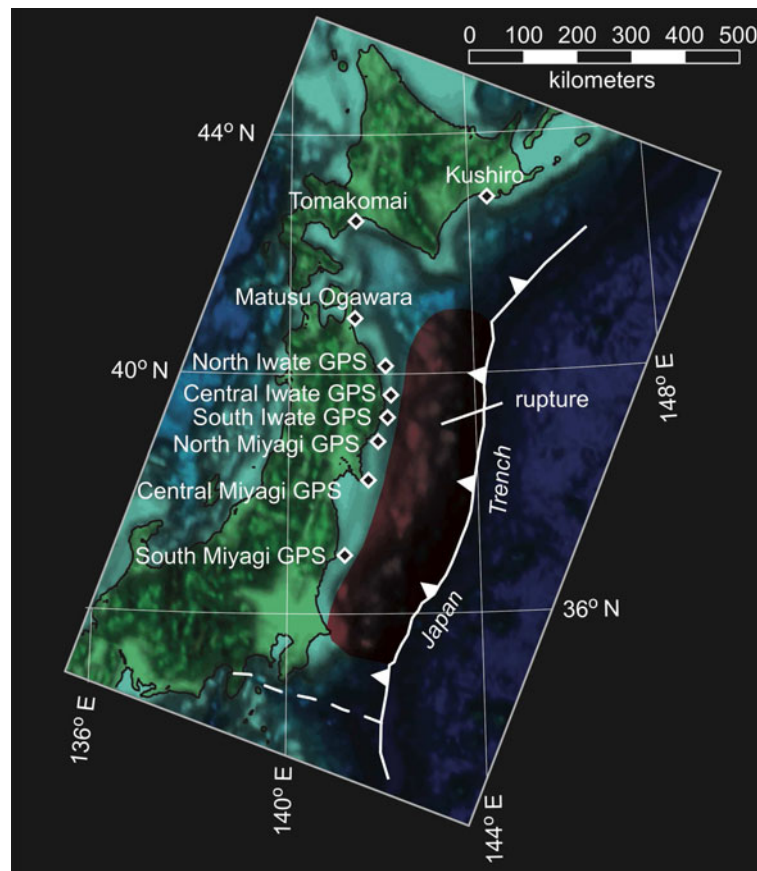
Figure 11
Locations of GPS buoy stations (Yamazaki *et al.* 2011a)

than those of the UCSB source (Fig. 12). While both sources are in good agreement with observations for the three northern buoys (a–c), the UA source is in much better agreement than the UCSB source for two of the three southern buoys (g and h), and the difference between both sources is not very significant in absolute terms at the southernmost buoy, i (which is near the area of the Fukushima nuclear power plant). For the middle three buoys (d–f), neither source matches the data as well as for the other buoys. However, except for the first (higher-frequency wave) crest that it underpredicts, the UA source predicts the long waveform more accurately than the UCSB source. Neither source is able to reproduce the shorter wave oscillations that were measured at the three middle buoys.

Note that our findings for the UCSB source results are somewhat similar to those of Yamazaki *et al.* (2011b), which show generally good agreement with

the buoy data, but for some stations (i.e., North and Central Miyagi) their simulations underpredict the observed amplitude, and for others (i.e., South Miyagi, which they refer to as the Fukushima GPS station) they overpredict the initial amplitude.

5.3. Transpacific Propagation and Dispersive Effects

The far-field propagation in the Pacific Ocean basin is simulated using the spherical FUNWAVE-TVD code in the $4'$ arc resolution ocean basin grid (Table 1; spanning 132°E–68°W and 60°S–60°N; Fig. 3), initialized by NHWAVE results at $t = 300$ s (obtained with time-dependent triggering specified on the seafloor). The simulation is run for 24 h of tsunami propagation, in order for waves to reach the most distant DART buoys and the South American coastline.
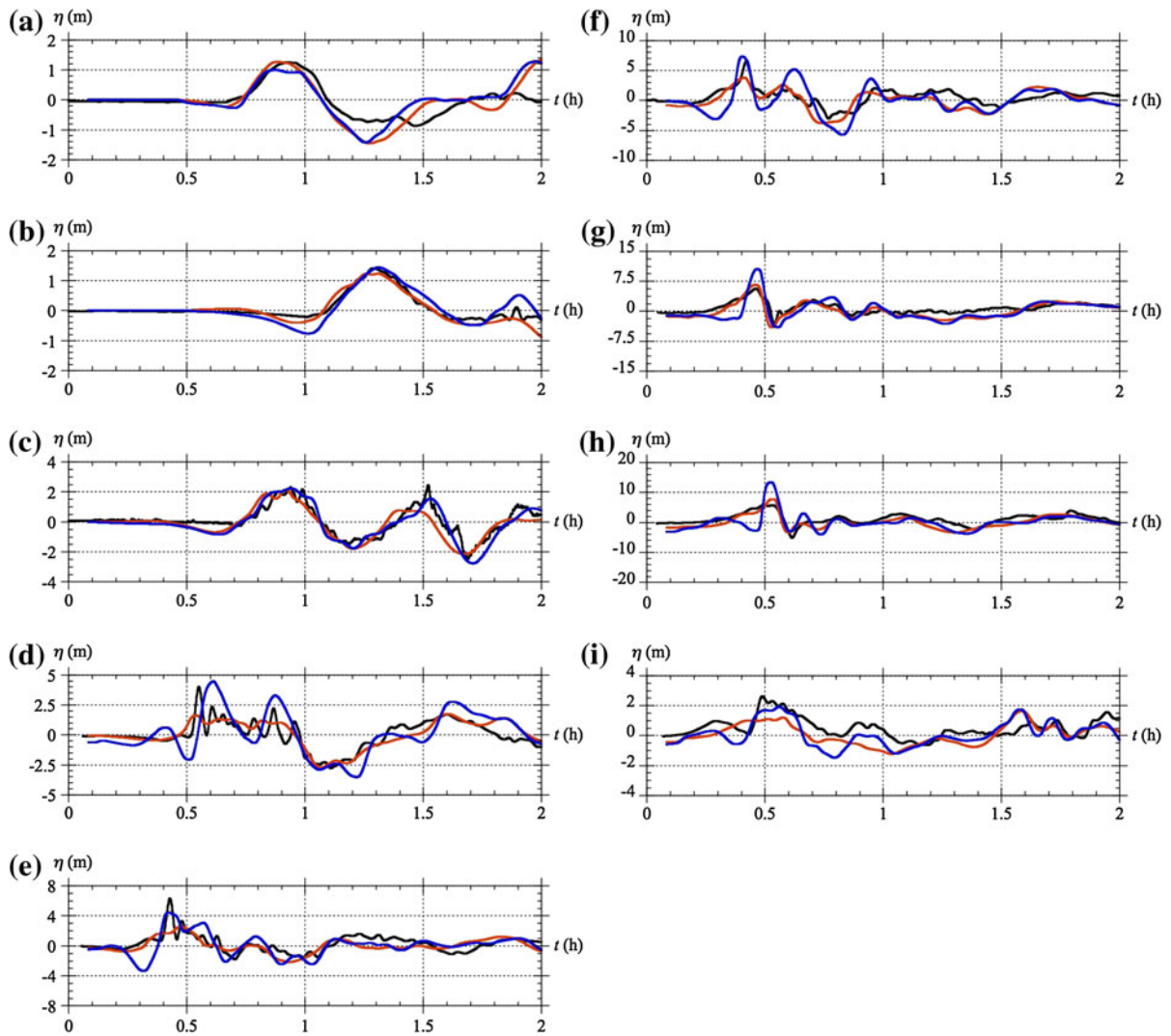
Figure 12
Surface elevations at GPS buoys near Japan as a function of time. Panels (**a**) to (*i*) are for stations located, from N to S (Figs. 4, 11), at: (**a**) Kushiro; (**b**) Tomakomai; (**c**) Matsu Ogawara; (**d**) North Iwate; (**e**) Central Iwate; (**f**) South Iwate; (**g**) North Miyagi; (**h**) Central Miyagi; (**i**) South Miyagi. Each panel compares observations (*black*) to computations for the: UCSB (M9) source (*blue*) and UA (M8.8) source (*red*). [*Note* source triggering in NHWAVE is time-dependent and specified on the seafloor]

Figure 13 shows a comparison of computed and measured surface elevations at the four DART buoys closest to Japan (i.e., No. 21413, 21418, 21401, and 21419; Fig. 3). Overall, results for both the UCSB and UA sources agree quite well with observations. The UCSB source, however, consistently overpredicts the leading wave crest elevation at each location and, more notably, overpredicts the amplitude of the leading wave troughs. Both the UA and UCSB sources predict that the wave arrives slightly sooner

than seen in observations, but this is more pronounced for the UCSB source. Figure 14 similarly shows a comparison of computed and measured surface elevations at four distant DART buoys (i.e., No. 51407, 46404, 32411, and 32412; Fig. 3). Similar to YAMAZAKI *et al*. (2011b, 2012), we find that at distant DART buoys the tsunami arrives earlier than observed (about 7–15 min). Hence, to allow for an easier comparison, slight time shifts have been added to simulations in the figure, in order to synchronize
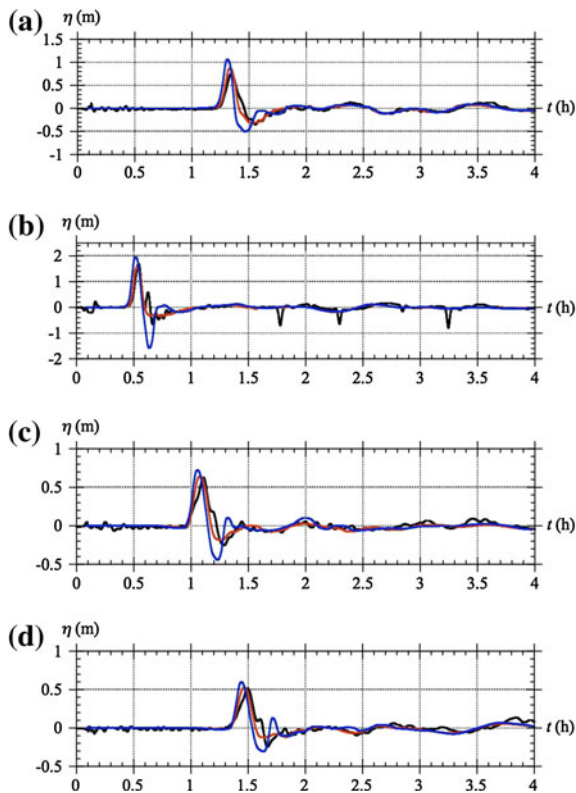
Figure 13

Surface elevation at DART buoys near Japan (Fig. 3) #: **a** 21413; **b** 21418; **c** 21401; and **d** 21419. Comparison between observations (*black*) and computations with FUNWAVE-TVD using the: UCSB source (*blue*); and the UA source (*red*). [*Note*, source triggering in NHWAVE is time-dependent and specified on the seafloor]

Figure 14

Surface elevation at DART buoys far from the source (Fig. 3) # ($\Delta t =$): **a** 51407 (+6.6 min); **b** 46404 (+7.2 min); **c** 32411 (+15.8 min); and **d** 32412 (+15.2 min). Comparison between observations (*black*) and computations with FUNWAVE-TVD using the: UCSB source (*red*), and UA source (*blue*). Times listed in *parentheses* indicate the time shift (Δt) added to simulation results in order to synchronize these with observations. [*Note* source triggering in NHWAVE is time-dependent and specified on the seafloor]

the first elevation wave with that observed. These only represent about 1.5 % of the tsunami propagation time to each buoy. Results from WATADA *et al.* (2011) suggest that this discrepancy is common with many tsunami models and may be attributed largely to the elasticity and self-gravity of the Earth. The predicted surface elevations at distant DART buoys generally agree reasonably well with observations (particularly in view of their smaller magnitude than for the DART buoys closest to Japan), and neither source appears to yield significantly different results, indicating that differences that appear may be determined by the model setup. The best agreement is found in Hawaii and in Oregon (e.g., No. 51407 and 46404); at the latter buoy the UA source matches the leading wave much better than the UCSB source. Both the UCSB and UA sources underpredict the
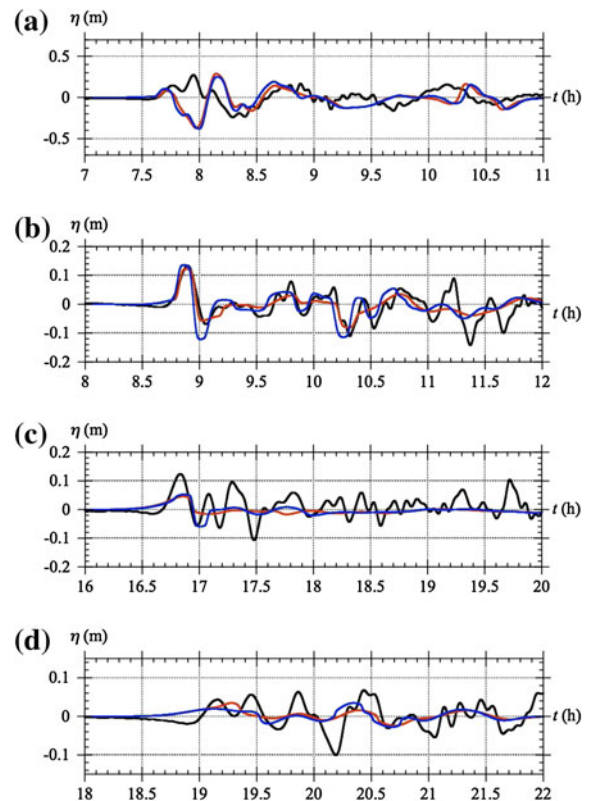
wave elevation similarly at DART stations near the South American shorelines (e.g., No. 32411 and 32412). Our results seem to agree better with measurements closest to Japan than those of YAMA-ZAKI *et al.* (2011b, 2012) who, for instance, underpredict the amplitude of the tsunami at DART buoy No. 21418 by about 50 %, whereas both the UA and UCSB sources used in our model reproduce the observations better. Alternatively, YAMAZAKI *et al.* (2011b, 2012) reproduce the waves measured at distant DART buoys perhaps slightly better. This may be related to the resolution of the respective models; our present simulations used a fairly coarse 4′ arc basin scale grid, as opposed to their 2′ arc resolution grid.
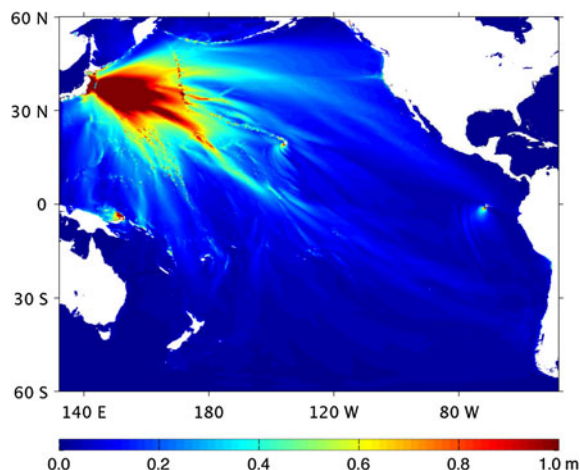
Figure 15

Envelope of maximum computed wave elevation with FUN-WAVE-TVD in the spherical (4′) Pacific grid using the UCSB source

Figure 16

Difference between the envelope of maximum wave elevation computed with FUNWAVE-TVD in the spherical (4′) Pacific grid using the UCSB source, with (as in Fig. 15) and without dispersion

Figure 15 shows the envelope of computed maximum wave elevation (for the UCSB source). The tsunami energy is seen to propagate across the ocean in some preferential directions associated with both the source characteristics and the ocean bathymetry, in which ridges may cause wave-guiding effects. This is particularly clear for the eastward propagation towards Northern California, around 40°N; large wave oscillations (nearly 4 m trough to crest) and damage were indeed observed at this latitude in Crescent City, CA.

The effect of dispersion on the tsunami transpacific propagation is finally assessed by re-running these simulations without dispersion terms in FUN-WAVE-TVD's equations, i.e., in NSW mode. Figure 16 shows a difference plot between the envelope of maximum surface elevation computed with (i.e., as in Fig. 15) and without dispersion. As could be expected from the short propagation distances and the coarse grid resolution, little dispersive effects can be seen in the near-field close to Japan. In the far-field, however, non-negligible differences with NSW results, of more than ±10 cm, can be seen in deep water, which may amount to 20–40 % of the tsunami amplitude at some locations. This is on the same order of magnitude as that of dispersive effects reported by IOUALALEN et al. (2007) for the 2004 Indian Ocean tsunami and justifies using a BM in the present case. A more detailed discussion and analysis of dispersive effects and their
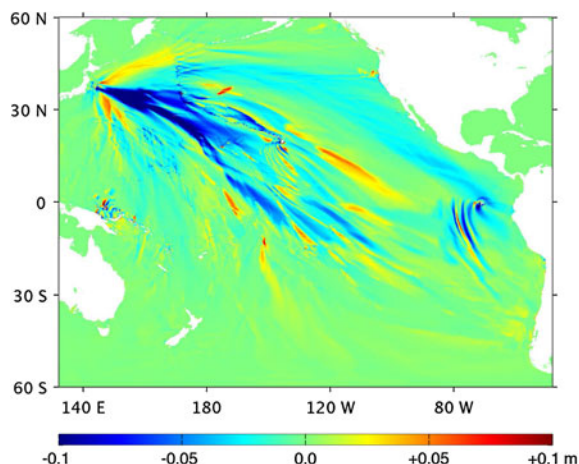
comparison to Coriolis force effects for the Tohoku 2011 event can be found in KIRBY et al. (2012).

Note, as we only consider here changes in maximum wave height due to dispersion, results do not show effects of dispersion on trailing waves such as noted by SAITO et al. (2011) at DART No. 21418. The dispersive tail, which is coarsely resolved in the DART buoy No. 21418 observations, does not appear in our simulations, whether using the UA or UCSB source (Fig. 13b), or any other finite-fault based sources that we attempted previously. We note, however, that the tsunami source used by SAITO et al. (2011) was based on an inversion of observed tsunami wave elevations only, while our modeling efforts have been solely from geophysical and seismic data, and have not been adjusted to fit wave observations. It is possible that seismic and geodetic inversions do not have sufficient resolution to produce these secondary waves, or more likely that a non-seismic contribution to the tsunami may be significant, such as from splay faulting or submarine mass failures. This will be the object of future work and will require field data to better constrain the potential seafloor mechanisms.

5.4. Runup and Inundation

We study the tsunami coastal impact on Japan, in terms of runup and inundation, using results of
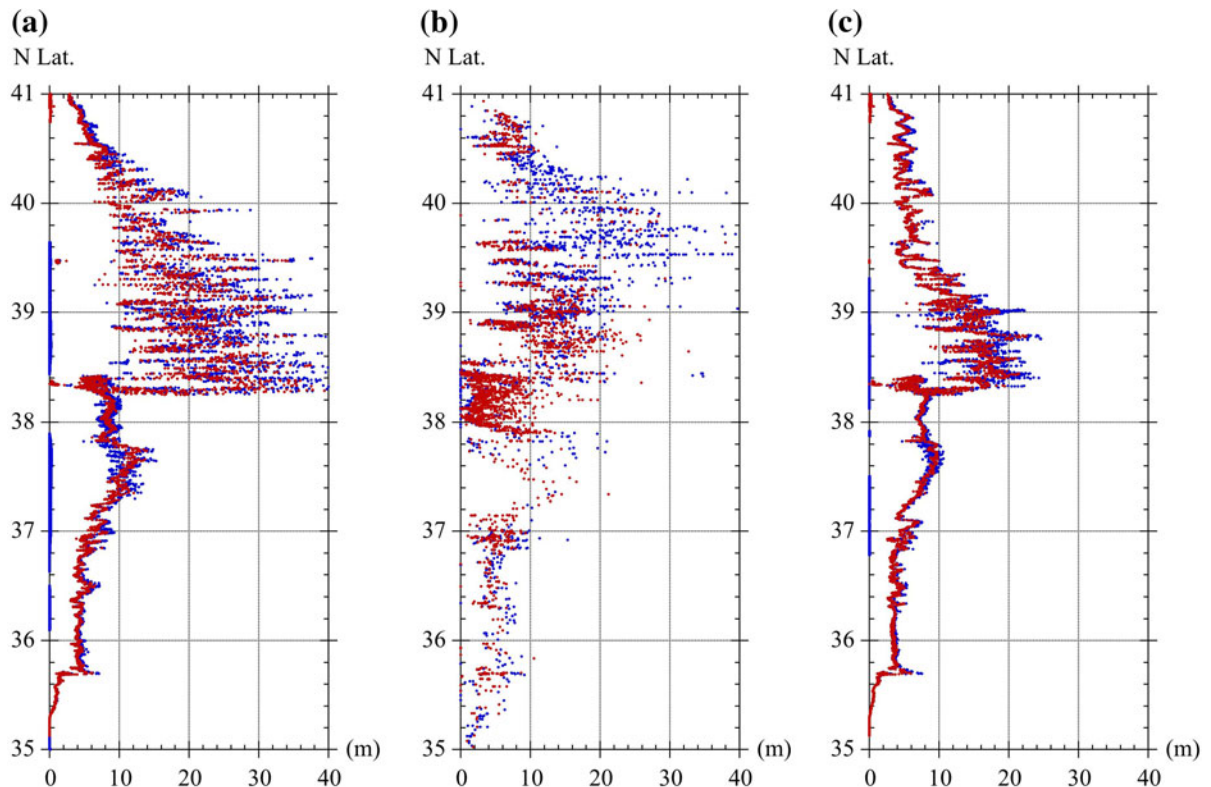
Figure 17
Runup (*blue circles*) and inundation height (*red dots*) along the Japanese coastline based on: **a** simulations with the M9 UCSB source; **b** field survey; and **c** simulations with the M8.8 UA source

simulations in the 250 m resolution coastal Grid (Table 1). Following the transition from the NHWAVE to the FUNWAVE-TVD 1,000 m regional grid at $t = 300$ s, we interpolate results from the latter grid onto the 250 m resolution coastal grid after 15 min. of tsunami propagation (i.e., 5 min. simulated with NHWAVE and 10 min. simulated with FUN-WAVE-TVD). The resulting initial condition is simulated for another 2 h in the coastal grid, which has 50 km wide sponge layers on the north, south, and east sides of the domain to prevent unwanted reflection. The bathymetry specified in the coastal grid is defined from the best publicly available data; thus, using linear interpolation, we combine the 500 m resolution JODC bathymetry along the Japanese coastline with 1″ arc ASTER topographic data.

Figure 17 shows runup (i.e., maximum elevation of wetted land) and inundation height (i.e., maximum wave elevation at shoreline) computed with

FUNWAVE-TVD in the coastal grid, for the UA and UCSB sources. We see that the observed runup and inundation values are well predicted in the region between 35° and 38.25°N, for both sources. Between 38.25° and 39°N, the UA source results agree quite well with the maximum observed values of runup and inundation height in the region, while the UCSB results overpredict both of these by almost a factor of 2. Between 39° and 39.5°N, this finding is reversed and the UA source results underpredict observations by almost a factor of 2, while the UCSB source results are in better agreement with observations (although still overpredicting these). Between 39.5° and 40.25°N, the runup is underpredicted for both sources. As indicated in the introduction, in view of the still insufficient resolution of the coastal grid, this could be due in part to effects of the complex bathymetry and topography in this part of the Japanese coastline, the Sanriku/Ria coast, which

could greatly enhance tsunami runup. Even at a 250 m resolution, the tsunami in most locations only inundated a few grid points onshore in the model. By contrast, in the south, the coastline is made of plains and, accordingly, runup and inundation values are well predicted by the model using either source (and almost identical).

In order to better predict runup in the north, one needs to represent the complex topography of the coastline in the model, by using a much finer grid (perhaps down to 30–50 m resolution). This would also require using a better resolved bathymetry than the 500 m dataset currently used and will be the object of future work. For this reason, we believe that with the current bathymetric data and 250 m coastal grid resolution, inundation results should be more reliable than runup, as they are predicted at the shoreline, which warrants a further analysis. This is done in Fig. 18, where computed inundations for both sources are directly compared to observed inundation values, north of 38°N. In this region, results for the UA source are in good agreement with observations, except between 39.2° and 40.2°N, where these are significantly underpredicted in the model. This is an area where the UA source may lack in tsunami generation, perhaps due to underpredicted seafloor deformations, but this could also be due to other phenomena not included in the coseismic sources (e.g., splay faults, submarine mass failures, etc.). By contrast, as before, the UCSB source significantly overpredicts the observed inundation up to 39.6°N and, like the UA source, underpredicts the inundation between 39.6° and 40.2°N, albeit by a smaller factor. The UCSB source thus overpredicts seafloor deformation between 38.25° and 39.6° and underpredicts it between 39.6° and 40.2°N, similar to the UA source. Overall, however, based on the inundation metrics, the UA source is seen to agree better with tsunami observations.
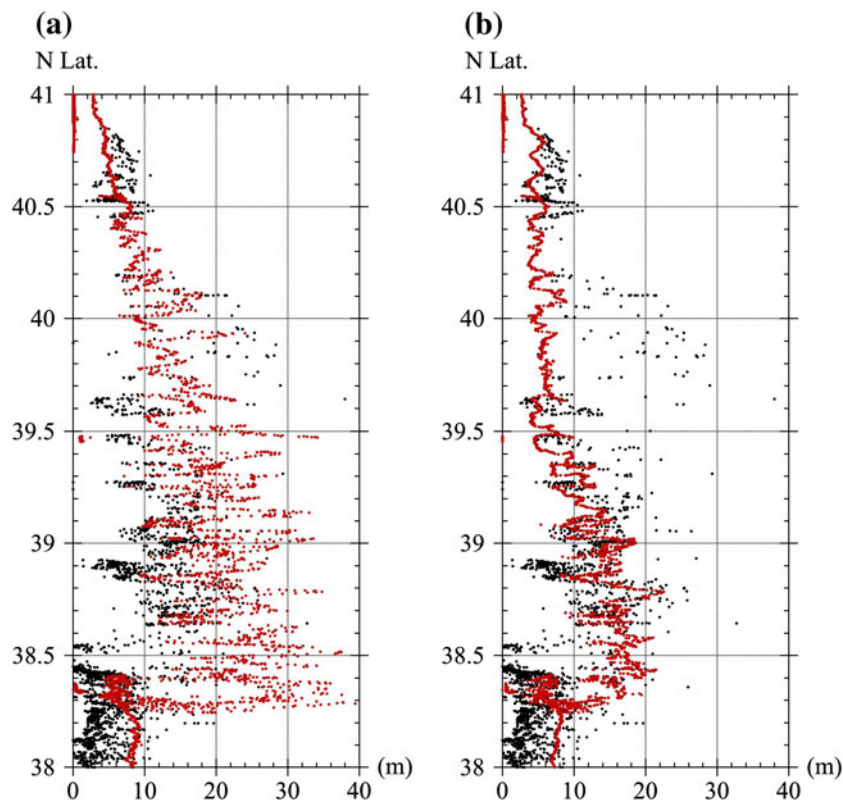

Figure 18
Zoom in Fig. 17 results north of 38°N. Inundation measured (*black dots*) and computed (*red*) with: **a** M9 UCSB source; and **b** M8.8 UA source

6. Summary

We simulated tsunami generation propagation, near-field (coastal), and far-field impact of the Tohoku 2011 tsunami, using the nonlinear and dispersive Boussinesq wave model FUNWAVE-TVD (in Cartesian or spherical coordinates), and compared results to field observations of surface elevation at DART buoys, GPS gauge buoys, and runup and inundation along the most impacted coastal area of Japan (from 35° to 41°N). FUNWAVE was initialized based on coseismic tsunami sources developed from seismic (UCSB; SHAO *et al.* 2011) or GPS data (UA) inversion. We used a series of nested model grids, with varying resolution (from 4′ in deep water down to 250 m nearshore) and size, and assessed effects on results of the inclusion of dispersive effects and model initialization method; namely, the triggering of tsunami sources in the propagation model: (i) either at once as a hot start, or with the spatiotemporal sequence derived from seismic inversion; and (ii) as a specified surface elevation or as a more realistic time and space-varying bottom boundary condition (in the latter case, we computed the initial tsunami generation up to 300 s using the nonhydrostatic model NHWAVE).

Present results showed that dispersive effects are negligible in the near-field, owing to the short propagation distances and coarse grid resolution, but may account for 20–40 % of tsunami amplitude in deep water, hence justifying the use of a Boussinesq model. When using finer coastal grids, however, incoming tsunami waves may propagate nearshore in the form of strongly dispersive undular bores (as was observed during the 2004 Indian Ocean tsunami; MADSEN *et al.* 2008), that will also require a model such as FUNWAVE for accurate modeling. The sensitivity of results to the three source triggering methods was assessed for the UCSB coseismic source. Comparing results at $t = 300$ s, significant differences were found in both surface elevation and wavelength, between the instantaneous method (i) and the two time-dependent methods (ii). Smaller differences were observed between the latter methods, with the time-triggering in NHWAVE resulting in slightly reduced maximum (positive or negative) elevations and in waveforms with less higher-

frequency oscillations than for the time-triggering in FUNWAVE-TVD. These results justify using the third more accurate and realistic method to compute the initial tsunami waveform (i.e., the time dependent bottom boundary condition in NHWAVE), which was done in all the applications.

The UA source is a new coseismic tsunami source developed here, based on inverting onshore and offshore geodetic data using 3D Finite Element Models (FEM) that simulate elastic dislocations along the plate boundary interface separating the stiff subducting Pacific Plate from the relatively weak forearc and volcanic arc of the overriding Eurasian plate. Standard sources based on seismic inversion often have very simple underlying fault models (such as OKADA 1985; UCSB), yielding deeper slip in homogeneous half-spaces, which may underpredict the amplitude of the tsunami in some areas and lag the wave in time. By contrast, in part due to the simulated weak forearc materials, the UA source produces significant shallow slip along the updip portion of the rupture near the trench that may enhance tsunami generation. Salient features of the observed tsunami far-field and coastal impact were well reproduced for both the UCSB and UA sources, but coastal impact was over- or under-estimated at some locations. Overall, however, results obtained for the UA source were found in better agreement with observations at nearshore GPS gauges and DART buoys, and at some distant DART buoys, than those for the UCSB source. Regarding the simulation of runup and inundation, it was concluded that the current finer resolution FUNWAVE grid was still too coarse at 250 m (as well as the underlying bathymetry at 500 m), to accurately simulate runup, particularly in the Sanriku/Ria area (39.5° and 40.25°N) where maximum impact (up to 40 m runup) occurred, which has complex bathymetry and topography that may require grids as small as 30–50 m for proper modeling. Inundation, however, was deemed less sensitive to grid resolution and used as a metric to assess the accuracy of simulation results along the Japan coast. Hence, it was found that both sources accurately predicted inundation observations south of 38°N. To the north, results for the UA source were found in good agreement with observations, except between 39.2° and 40.2°N, where these were underpredicted.

In addition to the complex coastline mentioned above, this is an area where the UA source may lack in tsunami generation, perhaps due to underpredicted seafloor deformations, but this could also be due to other phenomena not included in the coseismic sources (e.g., splay faults, submarine mass failures, etc.). By contrast, the UCSB source significantly overpredicted observed inundations up to 39.6°N and, like the UA source, underpredicted the inundation between 39.6° and 40.2°N, albeit by a smaller factor.

Overall, based on the inundation metric along the coast and the agreement with GPS and DART buoy data, results using the newly proposed FEM UA source were found to agree better with tsunami observations, in both the near- and far-field, than those using the UCSB source. As indicated, the UA source may need additional refinements to better explain observations between 39.2° and 40.2°N; these are currently in development and expected to be available in the near future. However, the current UA source already accounts for geologic inhomogeneities (both material and geometrical), which are neglected in Okada-based approaches (which it in fact generalizes) and thus, when combined with accurate tsunami generation and propagation models, as reported here, it has the potential to better explain the large runup and inundation observed to the north of the impacted area, as a result of coseimsic processes.

Finally, there were early indications that Submarine Mass Failures (SMFs) may have been triggered in the Japan trench by the Tohoku-Oki M9 earthquake. The inclusion in tsunami generation models of such SMF sources (as was done, e.g., in WATTS *et al.* 2003; DAY *et al.* 2005; TAPPIN *et al.* 2008) may help further explain some of the large runups not accounted for in the present work. The most likely candidate SMF tsunami source would be a large failure or deformation near the trench axis (FUJIWARA *et al.* 2011; ITO *et al.* 2011).

REFERENCES

ABADIE S, HARRIS JC, GRILLI ST, FABRE R (2012) Numerical modeling of tsunami waves generated by the flank collapse of the Cumbre Vieja Volcano (La Palma, Canary Islands): tsunami source and near field effects. Journal of Geophysical Research 117(C07646), doi:10.1029/2011JC007646

ABAQUS (2009) Abaqus. Dassault Systemes Simulia Corp., Providence, RI, 6.9-EF edn, URL: http://www.simulia.com

ABE H, SUGENO Y, CHIGAMA A (1990) Estimation of the height of the Sanriku Jogan 11 earthquake-tsunami (A.D. 869) in the Sendai Plain. Zisin [Earthquakes] 43:513–525

AMANTE C, EAKINS BW (2009) ETOPO1 one arc-minute global relief model: Procedures, data sources and analysis. NOAA Technical Memorandum NESDIS NGDC-24:19 pp

AMMON CJ, LAY T, KANAMORI H, CLEVELAND M (2011) A rupture model of the great 2011 Tohoku earthquake. Earth Planets Space 63:693–696, doi:10.5047/eps.2011.05.015

ASTER R, BORCHERS B, THURBER C (2005) Parameter estimation and inverse problems. Elsevier Academic Press, Amsterdam

BIRD P (2003) An updated digital model of plate boundaries. Geochemistry Geophysics Geosystems 4(3):55 pp., doi:10.1029/2001GC000252.

CHEN Q (2006) Fully nonlinear Boussinesq-type equations for waves and currents over porous beds. Journal of Engineering Mechanics 132:220–230

CHEN Q, KIRBY JT, DALRYMPLE RA, KENNEDY AB, CHAWLA A (2000) Boussinesq modeling of wave transformation, breaking and runup. II: Two horizontal dimensions. J Waterway, Port, Coastal and Ocean Engrng 126:48–56

CHEN Q, KIRBY JT, DALRYMPLE RA, SHIF, THORNTONEB (2003) Boussinesq modeling of longshore currents. Journal of Geophysical Research 108(C11):3362, doi:10.1029/2002JC001308

DAY SJ, WATTS P, GRILLI ST, KIRBY J (2005) Mechanical models of the 1975 kalapana, hawaii earthquake and tsunami. Marine Geology 215(1-2):59–92, doi:10.1016/j.margeo.2004.11.008

DEMETS C, GORDON R, ARGUS D (1994) Effect of recent revisions to the geomagnetic reversal time scale on estimates of current plate motions. Geophysical Research Letters 21:2191–2194

DZIEWONSKI AM, ANDERSON DL (1981) Preliminary reference Earth model. Physics of the Earth and Planetary Interiors 25(4):297–356

ENET F, GRILLI ST (2007) Experimental study of tsunami generation by three-dimensional rigid underwater landslides. Int J Num Meth Fluids 133:442–454

ERDURAN KS, ILIC S, KUTIJA V (2005) Hybrid finite-volume finite-difference scheme for solution of Boussinesq equations. Int J Num Meth Fluids 49:1213–1232

FUJII Y, SATAKE K, SAKAI S, SHINOHARA M, KANAZAWA T (2011) Tsunami source of the 2011 off the Pacific coast of Tohoku Earthquake. Earth Planets Space 63:815–820

FUJIWARA T, KODAIRA S, NO T, KAIHO Y, TAKAHASHI N, KANEDA Y (2011) Tohoku-Oki earthquake: Displacement reaching the trench axis. Science 334:1240

Geospatial Information Authority of Japan (2011) The 2011 off the Pacific coast of Tohoku Earthquake: Crustal Deformation and Fault Model (Preliminary), http://www.gsi.go.jp/cais/topic110313-index-e.html

GICA E, SPILLANE M, TITOV V (2007) Tsunami hazard assessment using Short-term Inundation Forecasting for Tsunamis (SIFT) tool. In: EASTEC International Symposium 2007—Dynamic Earth: its Origin and Future, Sendai, Japan

GICA E, SPILLANE M, TITOV V, CHAMBERLIN C, NEWMAN J (2008) Development of the forecast propagation database for NOAA's Short-term Inundation Forecast for Tsunami (SIFT). Tech. rep., NOAA Tech. Memo. OAR PMEL-139,89 pp

GONZALEZ FI, MILBURN HM, BERNARD EN, NEWMAN JC (1998) Deep-ocean Assessment and Reporting of Tsunamis (DART): brief overview and status report. In: Proceedings of the International Workshop on Tsunami Disaster Mitigation, Tokyo, Japan, URL: http://www.ndbc.noaa.gov/dart/brief.shtml

GOTTLIEB S, SHU CW, TADMOR E (2001) Strong stability-preserving high-order time discretization methods. SIAM Review 43:89–112

GRILLI S, IOUALALEN M, ASAVANANT J, SHI F, KIRBY J, WATTS P (2007) Source constraints and model simulation of the December 26, 2004 Indian Ocean tsunami. Journal of Waterway Port Coastal and Ocean Engineering 133(6):414–428, doi:10.1061/(ASCE)0733-950X(2007)133:6(414)

GRILLI S, DUBOSQ S, POPHET N, PRIGNON Y, KIRBY J, SHI F (2010) Numerical simulation and first-order hazard analysis of large co-seismic tsunamis generated in the Puerto Rico trench: near-field impact on the north shore of Puerto Rico and far-field impact on the us east coast. Natural Hazards and Earth System Sciences 10:2109–2125, doi:10.5194/nhess-2109-2010

HASEGAWA A, UCHIDA N, IGARASHI T, MATSUZAWA T, OKADA T, MIURA S, SUWA Y (2007) Asperities and quasi-static slips on the subducting plate boundary east of Tohoku, Northeast Japan. In: TH Dixon and JC Moore (ed) The seismogenic zone of subduction thrust faults, Columbia University Press, New York, pp 451–475

HATORI T (1975) Tsunami magnitude and wave source regions of historical Sanriku tsunamis in Northeast Japan. Bulletin of Earthquake Research Institute 50:397–414

HAYASHI Y, TSUSHIMA H, HIRATA K, KIMURA K, MAEDA K (2011) Tsunami source area of the 2011 off the Pacific coast of Tohoku Earthquake determined from tsunami arrival times at offshore observation stations. Earth Planets Space 63:809–813

HUGHES K, MASTERLARK T, MOONEY W (2010) Poroelastic stress-coupling between the M9.2 2004 Sumatra-Andaman and M8.7 2005 Nias earthquakes. Earth and Planetary Science Letters 293:289–299, doi:10.1016/j.epsl.2010.02.043

HYPRE (2006) High Performance Preconditioners. User's Manual, software version 2.0.0. UCRL-CODE-222953. Center for Applied Scientific Computing, Lawrence Livermore National Laboratory

IDE S, BALTAY A, BEROZA G (2011) Shallow dynamic overshoot and energetic deep rupture in the 2011 Mw 9.0 Tohoki-Oki earthquake. Science doi:10.1126/science.1207020

IOC/UNESCO (2011) Casualties by the earthquake and tsunami of March 11, 2011. Bulletin No 29 (9/30/2011), Intergovernmental Oceanographic Commission. URL: http://www.ngdc.noaa.gov/hazard/tsunami/pdf/

IOUALALEN M, ASAVANANT J, KAEWBANJAK N, GRILLI S, KIRBY J, WATTS P (2007) Modeling the 26th December 2004 Indian Ocean tsunami: Case study of impact in Thailand. Journal of Geophysical Research 112(C07024), doi:10.1029/2006JC003850

ITO Y, et al. (2011) Frontal wedge deformation near the source region of the 2011 Tohoku-Oki earthquake. Geophysical Research Letters 38:L000G05, doi:10.1029/2011GL048355

JI C, WALD DJ, HELMBERGER DV (2002) Source description of the 1999 Hector Mine, California, earthquake, part I: Wavelet domain inversion theory and resolution analysis. Bulletin of the Seismological Society of America 92:1192–1207

KARLSSON J, SKELTON A, SANDEN M, IOUALALEN M, KAEWBANJAK N, and J ASAVANANT NP, VON MATERN A (2009) Reconstructions of the coastal impact of the 2004 Indian Ocean tsunami in the Khao Lak area, Thailand. Journal of Geophysical Research 114(C10023), doi:10.1029/2009JC005516

KATO T, TERADA Y, ITO K, HATTORI R, ABE T, MIYAKE T, KOSHIMURA S, NAGAI T (2005) Tsunami due to the 2004 September 5th off the Kii peninsula earthquake, Japan, recorded by a new GPS buoy. Earth Planets Space 57:297–301

KENNEDY AB, CHEN Q, KIRBY JT, DALRYMPLE RA (2000) Boussinesq Modeling Of Wave Transformation, Breaking, And Run-Up. I: 1D. J Waterway, Port, Coastal And Ocean Engrng 126(1): 39–47

KENNEDY AB, KIRBY JT, CHEN Q, DALRYMPLE RA (2001) Determination of inverse depths using direct Boussinesq modelling. Wave Motion 33:225–243

KIM DH, LYNETT PJ (2011) Dispersive and nonhydrostatic pressure effects at the front of surges. Journal of Hydraulic Engineering 137(7):754–765, doi:10.1061/(ASCE)HY.1943-7900.0000345

KIRBY JT, POPHET N, SHI F, GRILLI ST (2009) Basin scale tsunami propagation modeling using boussinesq models: Parallel implementation in spherical coordinates. In Proc WCCE-ECCE-TCCE Joint Conf on Earthquake and Tsunami (Istanbul, Turkey, June 22-24) paper 100:(published on CD)

KIRBY JT, SHI F, HARRIS JC, GRILLI ST (2012) Sensitivity analysis of trans-oceanic tsunami propagation to dispersive and Coriolis effects. Ocean Modeling (in revision):42 pp.

KOPER KD, HUTKO AR, LAY T, AMMON CJ, KANAMORI H (2011) Frequency-dependent rupture process of the 11 March 2011 Mw 9.0 Tohoku earthquake: Comparison of short-period P wave backprojection images and broadband seismic rupture models. Earth Planets Space 58:1–4

KOWALIK Z, MURTY TS (1993) Numerical modeling of ocean dynamics. World Scientific Pub.

LAY T, AMMON C, KANAMORI H, XUE L, KIM M (2011a) Possible large near-trench slip during the 2011 Mw 9.0 off the Pacific coast of Tohoku Earthquake. Earth Planets Space 63:687–692

LAY T, YAMAZAKI Y, AMMON CJ, CHEUNG KF, KANAMORI H (2011b) The great 2011 Earthquake off the Pacific coast of Tohoku (Mw 9.0): Comparison of deep-water tsunami signals with finite-fault rupture model predictions. Earth Planets Space 63:797–801

LIANG Q, MARCHE F (2009) Numerical resolution of well-balanced shallow water equations with complex source terms. Advances in Water Resources 32:873–884

MA G, SHI F, KIRBY JT (2012) Shock-capturing non-hydrostatic model for fully dispersive surface wave processes. Ocean Modeling 43-44:22–35

MADSEN PA, FUHRMAN DR, SCHÄFFER HA (2008) On the solitary wave paradigm for tsunamis. J Geophys Res 113(C12012), doi:10.1029/2008JC004932

MASTERLARK T (2003) Finite element model predictions of static deformation from dislocation sources in a subduction zone: Sensitivities to homogeneous, isotropic, Poisson-solid, and half-space assumptions. J Geophys Res 108(B11):17pp, doi:10.1029/2002JB002296

MASTERLARK T, HUGHES K (2008) The next generation of deformation models for the 2004 M9 Sumatra-Andaman Earthquake. Geophysical Research Letters 35:5 pp, doi:10.1029/2008GL035198

MINOURA K, IMAMURA F, SUGAWARA D, KONO Y, IWASHITA T (2001) The 869 Jogan tsunami deposit and recurrence interval of large-scale tsunami on the Pacific coast of northeast Japan. Journal of Natural Disaster Science 23(2):83–88

MORI N, TAKAHASHI T, The 2011 Tohoku Earthquake Tsunami Joint Survey Group (2012) Nationwide Post Event Survey and Analysis of the 2011 Tohoku Earthquake Tsunami. Coastal Engineering Journal 54(1):1250001.

MORI N, TAKAHASHI T, YASUDA T, YANAGISAWA H (2011) Survey of 2011 Tohoku earthquake tsunami inundation and run-up. Geophysical Research Letters 38(L00G14):6 pp., doi:10.1029/2011GL049210

OKADA Y (1985) Surface deformation due to shear and tensile faults in a half space. Bulletin of the Seismological Society of America 75(4):1135–1154

OZAWA S, NISHIMURA T, SUITO H, KOBAYASHI T, TOBITA M, IMAKIIRE T (2011) Coseismic and postseismic slip of the 2011 magnitude-9 Tohoku-Oki earthquake. Nature 475(7356):373–376, doi:10.1038/nature10227

PARARAS-CARAYANNIS G (2011) Tsunamigenic source mechanism and efficiency of the March 11, 2011 Sanriku earthquake in Japan. Science of Tsunami Hazards 30(2):126–152

POLLITZ F, BÜRGMANN R, BANERJEE P (2011) Geodetic slip model of the 2011 M9.0 Tohoku earthquake. Geophysical Research Letters 38:L00G08

RYAN W, CARBOTTE S, COPLAN J, O'HARA S, MELKONIAN A, ARKO R, WEISSEL R, FERRINI V, GOODWILLIE A, NITSCHE F, BONCZKOWSKI J, ZEMSKY R (2009) Global multi-resolution topography synthesis. Geochem Geophys Geosyst 10(Q03014), doi:10.1029/2008GC002332

SAITO T, ITO Y, INAZU D, HINO R (2011) Tsunami source of the 2011 Tohoku-oki earthquake, Japan: Inversion analysis based on dispersive tsunami simulations. Geophysical Research Letters 38:L00G19, doi:10.1029/2011GL049089

SATAKE K (1995) Linear and nonlinear computations of the 1992 Nicaragua earthquake tsunami. Pure Appl Geophys 144:455–470

SATO M, ISHIKAWA T, UJIRARA N, YOSHIDA S, FUJITA M, MOCHIZUKI M, ASADA A (2011) Displacement above the hypocenter of the 2011 Tohoku-Oki Earthquake. Science 332:1395, doi:10.1126/science.1207401

SAWAI Y, SHISHIKURA M, KOMATSUBARA J (2008) A study of paleotsunami using hard corer in Sendai plain (Sendai City, Natori City, Iwanuma City, Watari Town, Yamamoto Town), Miyagi, Japan. Geological Survey of Japan, National Institute of Advanced Industrial Science and Technology Tsukuba, Japan URL: http://unit.aist.go.jp/actfault-eq/english/reports/h19seika/index.html

SENO T, SAKURAI T, STEIN S (1996) Can the Okhotsk plate be discriminated from the North American plate? Journal of Geophysical Research 101:11,305–11,316

SHAO G, LI X, JI C, MAEDA T (2011) Focal mechanism and slip history of 2011 Mw 9.1 off the Pacific coast of Tohoku earthquake, constrained with teleseismic body and surface waves. Earth Planets Space 63:559–564

SHI F, KIRBY JT, HARRIS JC, GEIMAN JD, GRILLI ST (2012) A high-order adaptive time-stepping TVD solver for Boussinesq modeling of breaking waves and coastal inundation. Ocean Modeling 43-44:36–51

SIMONS M, MINSON S, SLADEN A, ORTEGA F, JIANG J, OWEN S, L MENG JPA, WEI S, CHU R, HELMBERGER D, KANAMORI H, HETLAND E, MOORE A, WEBB F (2011) The 2011 Magnitude 9.0 Tohoku-Oki Earthquake: Mosaicking the Megathrust from Seconds to Centuries. Science doi:10.1126/science.1206731

TAPPIN D, WATTS P, GRILLI S (2008) The Papua New Guinea tsunami of 1998: anatomy of a catastrophic event. Natural Hazards and Earth System Sciences 8:243–266.http://www.nat-hazards-earth-syst-sci.net/8/243/2008/

TEHRANIRAD B, SHI F, KIRBY JT, HARRIS JC, GRILLI ST (2011) Tsunami benchmark results for fully nonlinear Boussinesq wave model FUNWAVE-TVD, Version 1.0. Tech. rep., No. CACR-11-02, Center for Applied Coastal Research, University of Delaware

The 2011 Tohoku Earthquake Tsunami Joint Survey Group (2011) Nationwide field survey of the 2011 off the Pacific coast of Tohoku earthquake tsunami. Journal of Japan Society of Civil Engineers 67(1):63–66

TITOV VV, GONZALEZ FI, BERNARD EN, EBLE MC, MOJFELD HO, NEWMAN JC, VENTURATO AJ (2005) Real-time tsunami forecasting: Challenges and solutions. Nat Hazards 35:35–41, doi:10.1007/s11069- 004-2403-3

TONELLI M, PETTI M (2009) Hybrid finite volume - finite difference scheme for 2DH improved Boussinesq equations. Coast Engrng 56:609–620

TSUSHIMA H, HIRATA K, HAYASHI Y, KIMURA YTK, SAKAI S, SHINOHARA M, KANAZAWA T, HINO R, MAEDA K (2011) Near-field tsunami forecasting using offshore tsunami data from the 2011 off the Pacific coast of Tohoku Earthquake Hiroaki Tsushima. Earth Planets Space 63:821–826

WANG H (2000) Theory of linear poroelasticity: With applications to geomechanics. Princeton University Press

WATADA S, SATAKE K, FUJII Y (2011) Origin of travel time anomalies of distant tsunami. In: AGU Fall Meeting 2011 poster NH11A

WATTS P, GRILLI ST, KIRBY JT, FRYER GJ, TAPPIN DR (2003) Landslide tsunami case studies using a Boussinesq model and a fully nonlinear tsunami generation model. Natural Hazards and Earth System Sciences 3:391–402

WEI G, KIRBY JT (1995) A time-dependent numerical code for extended Boussinesq equations. Journal of Waterway, Port, Coastal and Ocean Engineering 120:251–261

WEI G, KIRBY JT, GRILLI ST, SUBRAMANYA R (1995) A fully nonlinear Boussinesq model for surface waves. I. Highly nonlinear, unsteady waves. Journal of Fluid Mechanics 294:71–92

YAMAGUCHI Y, KAHLE A, TSU H, KAWAKAMI T, PNIEL M (1998) Overview of advanced space borne thermal emission and reflection radiometer (ASTER). IEEE Trans Geosci Remote Sensing 36:1062–1071

YAMAMOTO S, KANO S, DAIGUCHI H (1998) An efficient CFD approach for simulating unsteady hypersonic shock-shock interference floes. Comput Fluids 27:571–580

YAMAZAKI Y, KOWALIK Z, CHEUNG KF (2009) Depth-integrated, nonhydrostatic model for wave breaking and run-up. International Journal of Numerical Methods in Fluids 61(5):473–497

YAMAZAKI Y, LAY T, CHEUNG K, YUE H, KANAMORI H (2011a) Modeling near-field tsunami observations to improve finite fault slip models for the 11 March 2011 Tohoku earthquake. Geophysical Research Letters 38:L049130, doi:10.1029/2011GL049130

YAMAZAKI Y, ROEBER V, CHEUNG KF, LAY T (2011b) Modeling the 2011 Tohoku-oki Tsunami and its Impacts on Hawaii. In: Proceedings of OCEANS 2011. Waikoloa, HI, USA. 9 pp.

YAMAZAKI Y, CHEUNG K, PAWLAK G, LAY T (2012) Surges along the Honolulu coast from the 2011 Tohoku tsunami. Geophysical Research Letters 39:L09604, doi:10.1029/2012GL051624

YUE H, LAY T (2011) Inversion of high-rate (1 sps) GPS data for rupture process of the 11 March 2011 Tohoku earthquake (Mw 9.1). Geophysical Research Letters 38:L00G09, doi: 10.1029/2011GL048700

ZHOU JG, GAUSON DM, MINGHAM CG, INGRAML DM (2001) The surface gradient method for the treatment of source terms in the shallow water equations. J Comp Phys 168:1–25